THE MATERIAL POINT METHOD FOR UNSATURATED SOILS

A. Yerro[1], E.E. Alonso[1] and N.M. Pinyol[1,2]

[1]*Department of Geotechnical Engineering and Geosciences, UPC*
[2]*International Centre for Numerical Methods in Engineering*

SUMMARY

The paper describes a three phase single point MPM formulation of the coupled flow (water and air) – mechanical analysis of geotechnical problems involving unsaturated soils. The governing balance and dynamic momentum equations are discretized and adapted to MPM characteristics: an Eulerian computational mesh and a Lagrangian analysis of material points. General mathematical expressions for the terms of the set of governing equations are given. A suction dependent elastoplastic Mohr-Coulomb model, expressed in terms of net stress and suction variables is implemented. The instability of a slope subjected to rain infiltration, inspired from a real case, is solved and discussed. The model shows the development of the initial failure surface in a region of deviatoric strain localization, the evolution of stress and suction states in some characteristic locations, the progressive large strain deformation of the slope and the dynamics of the motion characterized by the history of displacement, velocity and acceleration of the unstable mass.

KEY WORDS: Large displacements, dynamics, unsaturated soils, slope stability, run-out

1. INTRODUCTION

Applications of unsaturated soil mechanics often involve large deformations. This is the case of collapse behaviour of low density soils or the unrestrained swelling of expansive clays. Rain induced instability of unsaturated slopes is a further example of large displacements. In this case the slide run-out is directly associated with the risk evaluation of the instability. Finite element methods find difficulties to reproduce large deformations, while particle-based methods and, in particular, the Material Point Method offers an interesting alternative.

The Material Point Method (MPM) (Sulsky *et al*., 1994) was developed to simulate large deformations in history-dependent materials. It combines the advantages of Eulerian (fixed finite element grid) and Lagrangian (moving material points) approaches of the media: mesh distortion is eliminated because the computational grid is fixed. The formulation is dynamic and automatically includes a no-slip contact algorithm. These features make MPM especially useful to solve problems involving large deformations and displacements, velocities and accelerations.

During the last decade, MPM has been applied to very different fields, such as ice dynamics (Sulsky *et al*., 2007), gas dynamics (Tan & Nairn, 2002) or fracture of wood (Nairn & Matsumoto, 2009). It is also receiving increasing attention to solve geotechnical problems, e.g. studies of granular flows (Więckowski *et al*., 1999; Bardenhagen & Kober, 2004), modelling of anchors placed in soil (Coetzee *et al*., 2005), landslides and slopes (Andersen & Andersen, 2010; Beuth *et al*., 2011; Yerro *et al*., 2014; Alonso *et al*., 2014), and retaining walls (Więckowski, 2004; Beuth, 2012). In most of them, the soil is considered as a single-phase material. More recently, the interaction between two phases (solid and fluid) has been formulated basically in two different manners, either adopting one set of material points (Zabala & Alonso, 2011; Jassim *et al*., 2012) (single-point formulation) or two sets (Abe *et al*., 2014; Wieckowski, 2013) (multiple-point formulation).

In this paper, the MPM formulation is extended to model unsaturated soil problems, where the soil is understood as a unique medium integrated by three distinct phases (solid, liquid and gas). All phases are combined in each material point and balance and momentum equations are formulated and numerically solved within the framework of a general purpose MPM code. The soil constitutive model is formulated in a net stress-suction framework. The method is applied to analyse the instability of a slope on unsaturated soil subjected to rain infiltration.

2. MULITPHASE PROBLEMS IN MPM

The basic MPM formulation for a 1-phase mechanical problem is described in (Sulsky & Schreyer, 1996), where the equation of dynamic momentum balance is discretized. In these simulations, one single set of material points is necessary to model the continuum media. This approach is shown schematically in Figure 1 as 1-

phase-1-point formulation. This formulation has a large number of applications, including the geotechnical field. However, in most real problems different phases coexist and interact within the same domain. The necessity of modelling multiphase problems has led some authors to develop different MPM formulations.

In order to simulate 2-phase problems, in which solid and fluid phases interact, two main formulations have been developed: those based on a 1-point formulation and those based on a 2-point formulation (see Fig.1).

The first one has been used by different authors (Zabala & Alonso, 2011; Jassim *et al*., 2012; Al-Kafaji, 2013) to solve problems in saturated porous media. In this approach each material point carries all the information of the saturated porous media and the pore pressure is considered as an additional variable. In this case, the material points move attached to the solid skeleton.

The second discretization for 2-phase problems has been presented more recently in Abe *et al*. (2014), Bandara (2013) and Wieckowski (2013). It can be defined as a 2-point formulation, where the solid skeleton and the liquid phase are represented separately by two sets of Lagrangian material points (Fig.1). The fluid phase is modelled as an independent material; therefore the solid-fluid medium can be viewed as the superposition of two continuous media. Thus, the material points that represent the fluid phase, e.g. water, can simulate both, water within the pores (in a saturated porous media) and free water. In this way, seepage problems and fluid-structure interactions can be naturally solved. However, the computational cost of this approach is high because the number of material points needed in a calculation is twice the number of a single-point formulation in those parts of the domain where both phases coexist.

When the problem requires the simulation of 3 different phases, the MPM formulation can be stated in different ways (see Fig.1). The first approach corresponds to the 1-point discretization extended from 2-phases to 3-phases. A second approach is the extension from 2-point to 3-point formulation, where each phase is represented by an independent set of material points. Moreover, a 3-phase 2-point formulation can also be defined as a third possible case where two phases (e.g. the fluids: liquid and gas) are represented by the same set of material points.

The purpose of this paper is to simulate the unsaturated porous media as a unique continuous media formed by three phases (the 3-phase-1-point formulation has been implemented). The two other sketched multiple-point possibilities would require two

or three sets of material points, which imply a large computational cost. Every material point represents a portion of the solid-liquid-gas mixture and it moves fixed to the solid skeleton carrying the water and the gas pressures as variables.

3. UNSATURATED POROUS MEDIA

The unsaturated porous media is assumed to be a combination of three different phases (*ph*): solid (*s*), liquid (*l*) and gas (*g*) (Fig. 2). The solid phase constitutes the solid skeleton of the media; meanwhile the liquid and the gas phases fill the voids. Moreover, the fluids have been considered as a mixture of two components (*c*): water (*w*) and dry air (*a*).

Considering a portion of the unsaturated domain, its total volume V can be written as:

$$V = \sum_{ph} V_{ph} = V_s + V_l + V_g \tag{1}$$

where V_{ph} is the partial volume of a phase and V_s, V_l and V_g are the partial volumes for the solid, liquid and gas phases. The partial volumes can be written as

$$V_{ph} = n_{ph} V \tag{2}$$

where n_{ph} is the volume fraction associated with each phase.

Taking into account the volumetric relations of porosity n, and the degree of saturation S_l,

$$n = \frac{V_l + V_g}{V_s} \tag{3}$$

$$S_l = \frac{V_l}{V_l + V_g} \tag{4}$$

the volume fraction of each phase can be written as

$$n_s = (1 - n) \quad ; \quad n_l = nS_l \quad ; \quad n_g = nS_g \tag{5}$$

where $S_g = (1 - S_l)$ is the gas degree of saturation.

The mass m of a volume V is calculated as the sum of the partial masses m_{ph} of each phase:

$$m = \sum_{ph} m_{ph} \tag{6}$$

Taking into account that each phase can be considered as a mixture of components, the total mass is the sum of the partial masses of the components in each phase m_{ph}^{c}.

$$m = \sum_{ph} \sum_{c} m_{ph}^{c} \tag{7}$$

Defining the mass fraction of a component in a phase as

$$\omega_{ph}^{c} = \frac{m_{ph}^{c}}{m_{ph}} \tag{8}$$

and considering equation (2), the mass of a component in a phase is given by

$$m_{ph}^{c} = \omega_{ph}^{c} m_{ph} = \omega_{ph}^{c} \rho_{ph} V_{ph} = \omega_{ph}^{c} \rho_{ph} n_{ph} V \tag{9}$$

where ρ_{ph} is the density of a phase. Finally, the density of the mixture ρ_m is defined by considering the volume fractions of each phase as:

$$\rho_m = \sum_{ph} n_{ph} \rho_{ph} = (1-n)\rho_s + nS_l \rho_l + nS_g \rho_g \tag{10}$$

where ρ_s, ρ_l and ρ_g are the densities of solid, liquid and gas phases.

4. GOVERNING EQUATIONS

The dynamic behaviour of an unsaturated porous media can be formulated by specifying a set of physical laws: the momentum balances, the mass balances, the energy balance and the first and second laws of thermodynamics. In the most common form of the finite element formulation, the relative accelerations of the liquid and gas phases are neglected and the equations are solved considering solid displacement, liquid pressure and gas pressure as the primary unknowns ($\mathbf{u}_s$-p_l-p_g formulation) (Xikui & Zienkiewicz, 1992).

However, in order to capture the physical response of the porous media under dynamic conditions, the numerical approach presented in this work takes into account the relative accelerations and relative velocities of the pore fluids. Here, the

144 velocities of each phase become the fundamental unknowns ($\mathbf{v}_s$-$\mathbf{v}_l$-$\mathbf{v}_g$ formulation)
145 (based on Jassim *et al*., 2012).

146 *4.1. General assumptions*

147 The following assumptions have been adopted in the coupled MPM formulation
148 described in this paper:
149 1) Isothermal conditions
150 2) No mass exchange between solid and fluid phases
151 3) There is mass exchange of air and water between liquid and gas phases
152 4) Solid grains are incompressible
153 5) Distribution of porosity in the soil is assumed smooth (see Eq. I.16 in Appendix
154 I)
155 6) Spatial variations of water and air mass are assumed small (see Eq. I.16 in
156 Appendix I)
157 7) Diffusion of water in liquid is neglected
158 8) Diffusion of air in gas is neglected

159 *4.2. Momentum balance equations*

160 The momentum balance equation of the liquid phase (per unit of liquid volume) and
161 the momentum balance of the gas phase (per unit of gas volume) can be written,
162 respectively, as follows:

163 $$\rho_l \mathbf{a}_l = \nabla p_l - \frac{nS_l \mu_l}{k_l}\left(\mathbf{v}_l - \mathbf{v}_s\right) + \rho_l \mathbf{b} \tag{11}$$

164 $$\rho_g \mathbf{a}_g = \nabla p_g - \frac{nS_g \mu_g}{k_g}\left(\mathbf{v}_g - \mathbf{v}_s\right) + \rho_g \mathbf{b} \tag{12}$$

165 where $\mathbf{a}_l$ and $\mathbf{a}_g$ are the acceleration of the liquid and gas phase; $\mathbf{v}_l$, $\mathbf{v}_g$ and $\mathbf{v}_s$ are the
166 total liquid, gas and solid velocities; p_l and p_g are the liquid and gas pressures, μ_l and
167 μ_g are the dynamic viscosities of the liquid and the gas; k_l and k_g are the intrinsic
168 permeabilities of the liquid and the gas and $\mathbf{b}$ is the body force vector. These
169 expressions describe a generalized Darcy's law.
170 Finally, the momentum balance equation of the mixture (per unit of volume of
171 mixture) can be written as:

$$\rho_s(1-n)\mathbf{a}_s + \rho_l n S_l \mathbf{a}_l + \rho_g n S_g \mathbf{a}_g = \nabla \cdot \boldsymbol{\sigma} + \rho_m \mathbf{b} \tag{13}$$

where $\boldsymbol{\sigma}$ is the total stress tensor of the mixture. The momentum balance of the mixture has been selected instead of the momentum of the solid phase for convenience because, in practice, the total stress is usually known, unlike the stresses acting on the solid skeleton.

4.3. Mass balance equations

Because the exchange of mass between fluid phases is enabled, the mass balance equations have been formulated for each component (solid, water, air) instead of for each phase (solid, liquid, gas). In this manner, the flux terms become simpler because the evaporation and condensation of water and the dissolution and liberation of air are balanced within each component balance.

The mass balance equation of a component can be written as:

$$\sum_{ph}\left[\frac{\partial}{\partial t}\left(\frac{m^c_{ph}}{V}\right) + \nabla \cdot \mathbf{j}^c_{ph}\right] = 0 \tag{14}$$

The first term in the sum is the time derivative of the partial mass m^c_{ph} per unit volume of porous media and the second one is the divergence of the fluxes. The external sources or sinks of mass might appear in the right side of the equation, but in this case they have not been considered.

The flux referred to a particular component $\mathbf{j}^c_{ph}$ is written as the sum of diffusive flux ($\mathbf{i}^c_{ph}$) and advective flux:

$$\mathbf{j}^c_{ph} = \mathbf{i}^c_{ph} + \left(\frac{m^c_{ph}}{V}\right)\mathbf{v}_{ph} \tag{15}$$

The diffusive fluxes (i.e. diffusion of water in the gas and the diffusion of air in the water) can be modelled by means of the Fick's law (Fick, 1855), written as:

$$\mathbf{i}^c_{ph} = -\rho_{ph}\mathbf{D}^c_{ph}\nabla\omega^c_{ph} \tag{16}$$

in which $\mathbf{D}^c_{ph}$ is the dispersion tensor which includes non advective flux caused by molecular diffusion and hydrodynamic dispersion.

Developing the expressions (14) and (15) (see Appendix I), the mass balance equation for the solid skeleton becomes the following expression which describes de material derivative of the porosity.

$$\frac{Dn}{Dt} = (1-n)\nabla \cdot \mathbf{v}_s \tag{17}$$

Water and air mass balance equations have also been expanded (see Appendix I) considering the fluid pressures (p_l and p_g) as state variables, leading to the following expressions:

$$n\frac{D\left(\omega_l^w \rho_l S_l + \omega_g^w \rho_g S_g\right)}{Dp_l}\dot{p}_l + n\frac{D\left(\omega_l^w \rho_l S_l + \omega_g^w \rho_g S_g\right)}{Dp_g}\dot{p}_g = \\ = -(1-n)\left(\omega_l^w \rho_l S_l + \omega_g^w \rho_g S_g\right)\nabla \cdot \mathbf{v}_s - n\left(\omega_l^w \rho_l S_l\right)\nabla \cdot \mathbf{v}_l - n\left(\omega_g^w \rho_g S_g\right)\nabla \cdot \mathbf{v}_g - \nabla \cdot \mathbf{i}_g^w \tag{18}$$

$$n\frac{D\left(\omega_g^a \rho_g S_g + \omega_l^a \rho_l S_l\right)}{Dp_l}\dot{p}_l + n\frac{D\left(\omega_g^a \rho_g S_g + \omega_l^a \rho_l S_l\right)}{Dp_g}\dot{p}_g = \\ = -(1-n)\left(\omega_g^a \rho_g S_g + \omega_l^a \rho_l S_l\right)\nabla \cdot \mathbf{v}_s - n\left(\omega_l^a \rho_l S_l\right)\nabla \cdot \mathbf{v}_l - n\left(\omega_g^a \rho_g S_g\right)\nabla \cdot \mathbf{v}_g - \nabla \cdot \mathbf{i}_l^a \tag{19}$$

where the dot on p_l and p_g indicates the variation in time of the liquid and gas pressure, respectively.

4.4. Constitutive equations

The soil constitutive model is formulated in a net stress-suction framework. The net stress $\boldsymbol{\sigma}_{net}$ is equal to the excess of total stress over gas pressure and the suction is the difference between gas pressure and liquid pressure,

$$\boldsymbol{\sigma}_{net} = \boldsymbol{\sigma} - p_g \mathbf{m} \tag{20}$$

$$s = p_g - p_l \tag{21}$$

where $\mathbf{m} = (1\ 1\ 1\ 0\ 0\ 0)^T$

For saturated conditions when $p_l > p_g$, Terzhaghi's effective stress should be recovered and suction is assumed to be zero. It is then convenient to define the model in terms of the following constitutive stresses:

$$\bar{\boldsymbol{\sigma}} = \boldsymbol{\sigma} - \max\left\{p_g, p_l\right\}\mathbf{m} \tag{22a}$$

$$s = \max\left\{p_g - p_l, 0\right\} \tag{22b}$$

The general form of a suitable stress-strain relationship can be written incrementally as:

$$\mathrm{d}\overline{\boldsymbol{\sigma}} = \mathbf{D} \cdot \mathrm{d}\boldsymbol{\varepsilon} + \mathbf{h}' \mathrm{d}s \tag{23}$$

in which **D** is the tangent matrix and **h'** is a constitutive vector. Both are defined by means of the constitutive model. d**ε** is the strain increment vector.

4.5. Hydraulic constitutive equations

The degree of saturation S_l is strongly dependent on pore liquid and gas pressures. There are a number of empirical equations that describe this characteristic for soil in the literature. In this work the well-known van Genuchten retention curve (Genuchten, 1980) has been implemented, where P_0 and λ are assumed constants:

$$S_l = S_{\min} + \left[1 + \left(\frac{s}{P_0}\right)^{\frac{1}{1-\lambda}}\right]^{-\lambda} \left(S_{\max} - S_{\min}\right) \tag{25}$$

It is also necessary to specify the dependence of the liquid permeability on the degree of saturation. Being k_{sat} the liquid permeability under saturated conditions, the Hillel expression (Hillel, 1971) has been adopted:

$$k_l = k_{sat}\left(S_l\right)^m \tag{26}$$

The power *m* typically takes values in range 2-4 (a value of 3 is used in this work).

In addition, the variation of water mass fraction in the gas phase can be calculated according to the psychometric law (Edlefson & Anderson, 1943) and the variations of air mass fraction in the liquid can be obtained via the Henry's law (Mackay & Shiu, 1981).

Finally, viscosity and density of the phases can also be written depending on the fluid pressures.

4.6. Mechanical constitutive model

There was an interest in examining the behaviour of unsaturated slopes subjected to rain infiltration. In addition to determining the conditions leading to the onset of instability, a main objective was to follow the run-out of the unstable mass and to

247 determine the travelled distance, velocities and accelerations. All of these variables
248 define the risk and the destructive power of landslides. The instability is essentially
249 governed by the evolution of apparent soil cohesion and friction angle with the
250 evolving suction. The shear strength of unsaturated soils has been examined by
251 several authors (Fredlund *et al*., 1978; Escario & Saez, 1986; Delage & Graham,
252 1996). In general, both cohesion and friction depend nonlinearly on suction. It has
253 also been found that it depends on the current degree of saturation (Han *et al*., 1995;
254 Vaunat *et al*., 2002), but this dependence has not been included here. The soil shear
255 strength is defined by a Mohr-Coulomb expression

256 $$\tau = c + \overline{\sigma} \tan\varphi \tag{27}$$

257 The strength parameters, c and φ, are written as follows:

258 $$c = c' + c_s \tag{28}$$

259 $$\varphi = \varphi' + \varphi_s \tag{29}$$

260 where c' and φ' correspond to the cohesion and friction angle for saturated
261 conditions. The second terms of equations (28) and (29) include the effect of suction
262 in the material strength. It is accepted that cohesion increases with suction up to a
263 maximum value $\Delta c_{\max}$ as:

264 $$c_s = \Delta c_{\max}\left(1 - e^{-B(s/p_{atm})}\right) \tag{30}$$

265 where p_{atm} is the atmospheric pressure. B controls the rate of variation of apparent
266 cohesion with suction. On the other hand, the friction angle is assumed to have a
267 linear dependence with suction depending on parameter A:

268 $$\varphi_s = A(s / P_{atm}) \tag{31}$$

269 Obviously, other expressions could be introduced.

270 In order to reduce the singularities of the Mohr-Coulomb yield surface, the
271 modifications proposed by Abbo & Sloan (1995) have been implemented. An
272 explicit sub-stepping algorithm with error control and a correction for the yield
273 surface drift have been applied (Potts & Gens, 1985) .

5. NUMERICAL IMPLEMENTATION OF THE MPM. UNSATURATED FORMULATION

5.1. Space discretization

MPM discretizes the media in two different frames. First, the continuum is divided into a finite number of subdomains represented by material points (*p*) (see Fig.3). Each material point moves attached to the solid skeleton, carrying all the information and providing a Lagrangian description. Considering the standard MPM approach, it is assumed that the whole mass of a material point is concentrated at the corresponding material point; the density of the mixture ρ_m can be expressed as:

$$\rho_m(\mathbf{x},t)=\sum_{p=1}^{Np} m_p \delta(\mathbf{x}-\mathbf{x}_p) \tag{32}$$

in which m_p and $\mathbf{x}_p$ are the mass and the position of the material point p, δ is the Dirac delta function, and N_p is the total number of material points. Moreover, in the 3-phase-1-point MPM formulation, it is also necessary to consider the density of each phase ρ_{ph} as:

$$\rho_{ph}(\mathbf{x},t)=\sum_{p=1}^{Np} \tilde{m}_{ph}^{p} \delta(\mathbf{x}-\mathbf{x}_p) \tag{33}$$

The relationship between m_p and the mass of each phase is given by the following expression:

$$m_p=\sum_{ph} m_{ph}^{p}=\sum_{ph} n_{ph}\tilde{m}_{ph}^{p} \tag{34}$$

The second discretization frame is an Eulerian computational mesh (see Fig.3). The momentum equations are solved in the nodes (*i*). The standard linear shape functions N_i provide the relationship between the nodes and any point of the domain as follows:

$$\mathbf{w}(\mathbf{x},t)=\sum_{i=1}^{Nn} \mathbf{w}_i(t) N_i(\mathbf{x},t) \tag{35}$$

with N_n being the total number of nodes and $\mathbf{w}_i$ a specific field, such as the displacement field, evaluated in the node *i*.

5.2. Discrete form of the momentum balance equations

The Galerkin method of weighted residuals (Galerkin, 1915) has been applied to obtain the weak form of the momentum balance equations (11,12,13) (see the derivation in Appendix II). The expressions (32), (33) and (35) have been used to discretize the integrals over the domain into the nodes of the computational mesh considering the information carried by the material points. The final system of equations is written as:

$$\tilde{\mathbf{M}}_{\mathbf{l}} \cdot \mathbf{a}_{\mathbf{l}} = \mathbf{F}_{\mathbf{l}}^{\mathbf{ext}} - \mathbf{F}_{\mathbf{l}}^{\mathbf{int}} - \mathbf{Q}_{\mathbf{l}} \cdot \left(\mathbf{v}_{\mathbf{l}} - \mathbf{v}_{\mathbf{s}} \right) \tag{36}$$

$$\tilde{\mathbf{M}}_{\mathbf{g}} \cdot \mathbf{a}_{\mathbf{g}} = \mathbf{F}_{\mathbf{g}}^{\mathbf{ext}} - \mathbf{F}_{\mathbf{g}}^{\mathbf{int}} - \mathbf{Q}_{\mathbf{g}} \cdot \left(\mathbf{v}_{\mathbf{g}} - \mathbf{v}_{\mathbf{s}} \right) \tag{37}$$

$$\mathbf{M}_{\mathbf{s}} \cdot \mathbf{a}_{\mathbf{s}} + \mathbf{M}_{\mathbf{l}} \cdot \mathbf{a}_{\mathbf{l}} + \mathbf{M}_{\mathbf{g}} \cdot \mathbf{a}_{\mathbf{g}} = \mathbf{F}^{\mathbf{ext}} - \mathbf{F}^{\mathbf{int}} \tag{38}$$

where $\mathbf{a_s}$, $\mathbf{a_l}$, and $\mathbf{a_g}$ and $\mathbf{v_s}$, $\mathbf{v_l}$, and $\mathbf{v_g}$ are the nodal acceleration and velocity vectors for each phase. $\mathbf{F_l^{ext}}$ and $\mathbf{F_g^{ext}}$ are the vector of the liquid and gas external forces, respectively and $\mathbf{F^{ext}}$ the vector of the external forces of the mixture. Internal forces are indicated by means the superscript "int". $\mathbf{Q_l}$ and $\mathbf{Q_g}$ are the liquid and gas dragging matrixes. $\mathbf{M}$ and $\tilde{\mathbf{M}}$ are mass matrices per unit volume. The mathematical expression for each term is properly defined in the Appendix II.

This dynamic formulation includes natural damping in the dragging terms. However, in some problems such as in homogenous linear elastic materials it is necessary to apply artificial damping in order to reduce numerical instabilities. In this formulation, an additional damping force has been considered for each phase in the momentum balance equations. It is proportional to the corresponding unbalanced force (proportional factor α) and it is opposite to the phase velocity. This can be understood as frictional force. High values of the proportional factor can be used in quasi-static problems to get faster the static solution. In dynamic problems, where the accelerations have an important role in the course of the calculation, this factor should be very small (0-5%) in order to approximate the correct solution.

The classical MPM approach suffers from a "cell crossing instability" due to a jump discontinuity in the gradient of linear shape functions when the internal forces are calculated in the nodes. In order to mitigate this inconsistency, a simple technique that requires a low computational cost has been applied. It was used previously by several authors (Zabala & Alonso, 2010; Al-Kafaji, 2013;). It arises from

considering that the stress on each element is constant and corresponds to the average of the stresses of the material points that are located within the cell. Then, Gauss integration can be adopted to calculate the internal forces (as in FEM). A single Gauss point with an averaged stress is adopted in the analysis performed. In the literature several authors proposed other techniques to overcome this difficulty. Bardenhagen & Kober (2004) proposed a particle characteristic function instead of a Dirac delta function; in this way the mass of each material point is distributed in a certain space. This results in a family of methods known as Generalized Interpolation Material Point (GIMP) methods, such as uniform GIMP (uGIMP) and the contiguous-particle GIMP (cpGIMP), in which the particle characteristic function associated with each material points is constant or time-dependent respectively (Steffen *et al.*, 2008). Other extensions of the MPM are the convected particle domain interpolation methods (CPDI1 and CPDI2) which are capable of tracking material point domains more accurately, especially for problems involving massive deformations (Sadeghirad *et al.*, 2011; Sadeghirad *et al.*, 2013; Kamojjala *et al.*, 2013). These techniques typically increase the computational cost compared with the standard MPM.

5.3. Time discretization

The solution of the momentum balance equations (36) to (38) is obtained in a set of discrete times t^k by means of an explicit time integration scheme, where Δt is the time step increment, k is the number of time steps and N_t is the total number of time steps at the end of the calculation:

$$t^{k+1} = t^k + \Delta t \qquad k = 1,..., N_t \in I \tag{39}$$

Since the acceleration terms are the unknowns of the system of equations, the Forward Euler scheme is used to update the velocities,

$$\mathbf{v}^{k+1} = \mathbf{v}^k + \Delta t \mathbf{a}^k \tag{40}$$

The Backward Euler scheme is adopted for the displacements

$$\mathbf{u}^{k+1} = \mathbf{u}^k + \Delta t \mathbf{v}^{k+1} \tag{41}$$

The discrete approximation of the solution at time t^k is indicated by the superscript k.

5.4. Computational cycle

The numerical procedure is described by the following steps, which are solved for each time increment:

1) The information carried by the material points, such as the velocity of each phase, is mapped on the computational mesh. Nodal mass is calculated using the shape functions and the mass matrices are formed. Internal forces of the gas phase, the liquid phase and the mixture are evaluated in the nodes.
2) Nodal non-advective fluxes of air in the liquid and the water in the gas are calculated.
3) The momentum balance of gas is solved and nodal accelerations of the gas phase are calculated.
4) The momentum balance of liquid is solved and nodal accelerations of the liquid phase are calculated.
5) The momentum balance of the mixture is solved using liquid accelerations and gas accelerations previously obtained in steps 3 and 4. Nodal accelerations of the solid skeleton are determined.
6) Material point velocities and nodal velocities are updated using the forward Euler scheme. Particle displacements are updated using backward Euler scheme.
7) Strain increments for the solid phase and volumetric strain rates for the fluid phases are calculated on the material points.
8) The mass balance of the water and the mass balance of the air are solved as a linear system of equations. The increments of water and gas pressure are obtained in the material points.
9) The constitutive stresses are updated using a material constitutive model.
10) The material properties are updated in material points. The material point volume is updated considering the increment of volumetric strain; porosity is updated with the mass balance equation of solid; the degree of saturation is updated considering the updated fluid pressures. Other properties can also be updated here, such as the permeabilities, viscosities or mass fractions.
11) The computational grid is initialised for the next step and the material points carry all the updated information.

6. RAINFALL EFFECTS ON AN EMBANKMENT SLOPE

391 *6.1. Case description*

392 The problem solved was inspired by a real case described in Alonso *et al.*, 2010.
393 Several road embankments of medium height (6-8 m) were subjected to heavy
394 rainfall immediately after the end of construction. In some slopes, shallow failures,
395 which damaged the road side shoulders, were observed. The slides moved
396 downwards an estimated distance of 2-4 m. The embankments were built in summer
397 time and the soil, a low to medium plasticity sandy clay, was compacted dry of
398 optimum. Compaction conditions were investigated and some suction controlled
399 direct shear tests were also carried out. The loss of strength upon soil saturation
400 could be established.

401 The slope simulated has a height of 7 m and an angle of 32,5º (Figure 4). The flat
402 upper and lower surfaces reproduce the actual embankment geometry. The
403 calculation was performed in three dimensions and plane strain conditions were
404 assumed. The thickness of the model is 0.4 m.

405 Figure 4 also shows the computational mesh, formed by tetrahedrons, and the
406 distribution of material points. Those are initially distributed within each element and
407 are initially located at the corresponding integration points of a 4-point Gaussian
408 quadrature. The computational mesh covers a larger volume to allow for the expected
409 large displacements associated with the slope instability.

410 MPM as well as FEM are mesh dependent. Some authors have discussed the
411 influence of the number of material points and the mesh size on the accuracy of the
412 solution (Buzzi *et al.*, 2008; Bandara, 2013). Buzzi *et al.* (2008) have shown that the
413 mesh size is more determinant than the number of material points. Moreover,
414 separation and splitting in an MPM discretization also depends on the mesh size
415 because the material points remain numerically “in contact” while they have a node
416 in common. This fact is due to the no-slip contact, which is naturally included in the
417 MPM formulation, and it may lead to non-physical increase of the stiffness of the
418 material when it tends to separate (Huang *et al.*, 2011). Although the degree of mesh
419 dependency has not been established in this case, the mesh has been refined and
420 made homogeneous in the region where the failure is expected in order to get
421 accurate results.

422 Other numerical parameters are presented in Table 1. In this calculation a small
423 value of damping (α =0.05) was adopted which may represent the friction that can
424 occur between grains. A low value allows capturing the acceleration of the mass

motion and reduces spurious numerical instabilities. A too high value of damping would slow down any movement of the soil.

Regarding boundary conditions, the lower boundary is fixed and horizontal displacements along vertical contours are prevented. Lateral and bottom contours are impervious for the liquid phase. A constant zero gas pressure in excess of atmospheric pressure is prescribed in all the boundaries (p_g = 0 kPa).

The initial stresses and pore pressures of the slope are in equilibrium with the gravity force and the prescribed suction (s_0 = 800 kPa) distributed along the slope surface, which is in contact with the atmosphere.

The rainfall induced wetting is modelled by applying a decrease of suction on the material points located along the ground surface from 800 to 0 kPa during 10 seconds. Afterwards, the saturated boundary condition (s = 0 kPa) is maintained constant on the ground surface during the entire simulation period. An essentially downward flow is generated in the embankment due to suction gradients.

The embankment soil is assumed to be homogeneous and the properties of the different phases forming the soil (solid-liquid-gas) are presented in Table 2. Neither water vapour nor dissolved gas have been taken into account in this calculation. Therefore the liquid phase is pure water and the gas phase is considered to be dry air.

The water saturated permeability of the embankment was increased to accelerate wetting times and to reduce the computational time.

The elasto-plastic suction-dependent Mohr-Coulomb model simulates the soil behaviour and the constitutive parameters are summarized in Table 3. A small cohesion (1 kPa) is assumed under saturated conditions to avoid numerical difficulties in zones of very low effective confinement. The friction angle at saturated conditions was found to be close to 20º in direct shear tests performed on recovered samples. These parameters lead to unstable conditions, in a limit equilibrium analysis, in a situation of full saturation of the slope and zero suction. The slope remains initially stable thanks to the additional strength induced by the suction which depends on parameters A, B and Δc_{max} (equations (30) and (31)). The estimated A value leads to a very small variation in friction with suction: less than 1º for the maximum range of change on suction (800 kPa). The selected B and Δc_{max} values leads to a progressive reduction of cohesion with suction from a value c = 67 kPa at the initial state (s = 800 kPa) to c'= 1 kPa for saturated conditions.

458 The parameters of the water retention curve, equation (25), are listed in Table 4.
459 The shape of the van Genuchten model is shown in Figure 5.

460 *6.2. Embankment response*

461 In order to analyse the embankment behaviour, attention will focus on four
462 material points located in the lower half of the embankment, close to the boundary
463 slope, at depths of 0.5 m and 1.7 m. These shallow depths have been selected since a
464 relatively shallow failure is expected in this case because the loss of suction is faster
465 the closer to the boundary subjected to rainfall. The points (S1, S2, D1 and D2) are
466 represented in Figure 6a. The evolution of suction may be followed in Figure 6.
467 Contour plots of equal suction, at five different times, are selected: $t_1 = 0$ s, $t_2 = 20$ s,
468 $t_3 = 35$ s, $t_4 = 130$ s and $t_5 = 200$ s.
469 The first 20 seconds result in a major change in suction if compared with the
470 initial state characterized by an essentially constant value (s = 700-800 kPa). The
471 initial ($t_1 = 0$ s) vertical suction gradient reflects flow equilibrium conditions in view
472 of the imposed boundary conditions.
473 Also shown in the figure are the contours of deviatoric plastic strain. High shear
474 strains begin to develop at the slope toe soon after the beginning of wetting. A shear
475 band defining a potential shallow failure surface at an average depth of 1.5 m is
476 already defined at this early time. However the material points S1, S2, D1 and D2
477 remain essentially on their original positions. The slope is still stable. A few seconds
478 later, $t_3 = 35$ s, the shear band is already well developed and a failure surface is
479 defined. The slope becomes unstable and this is shown by the new positions of the
480 control points (Figure 6e). The displacement vector of point S2 shows that the central
481 part of the slope surface is having the maximum motion. The sliding mechanism is
482 also appreciated by the successive shapes of the slope as wetting continues to
483 increase. Soil masses located in the central and upper parts of the slope slide down
484 and pass over the material points located in the slope toe (point S1) which
485 experiences small displacements. The lowest point, D2, remains motionless because
486 it is located below the shear band.
487 It is also interesting to check that small positive water pressure (negative values of
488 suction in the figure) can be observed at some material points close to the bottom
489 boundary on the right side of the embankment, at times t_4 and t_5 (sketched in Figures
490 6g and 6i).

The final run-out can be quantified to be 2.5 m, if it is defined as the distance between the initial toe of the slope and the toe of the final geometry.

The wetting process is also illustrated in Figures 7 and 8. Figure 7 shows the evolution of "green field" suction for the left and right boundaries. We understand "green field" conditions, in the context of this example, as the conditions of the upper and lower horizontal "half spaces" in the absence of the presence of the slope. This condition is approximated by the left and right vertical boundaries of the example. The fast reduction of suction on the upper parts of the soil is well illustrated in the plots of Figure 7. Note that small positive pore water pressures are calculated in the lower part of the slope at $t_5 = 200$ s. Saturation is faster in this part of the slope. This is a consequence of the position of the impervious bottom boundary, which is closer to the ground surface (5 m below the surface) than on the left side (12 m below the surface). At the end of the calculation period the water still moves downwards in the left portion of the domain. However, on the left side water begins to accumulate on the lower part and the flow is directed towards the right, following pressure gradients.

Figure 8 shows the evolution of liquid pressure and the degree of saturation of points S1, S2, D1 and D2. Note that the plots of Figures 8a and 8b are directly related between them by the water retention relationship. According to the initial suction distribution, the degree of saturation at $t_1 = 0$ s is approximately 0.758. Points located at the same depth have similar wetting evolution. The reduction of suction is faster in shallow points (S1, S2) than in deeper points (D1, D2). As the calculation proceeds the degree of saturation increases and approaches almost fully saturated conditions at the end of the calculation period. However, significant suctions remain inside the embankment at this time (Figure 6i).

6.3. Stress-suction-time

The stress evolutions have been analysed for the four control points (S1, S2, D1 and D2) and are presented in Figures 9, 10 and 11. Figure 9 shows the evolution of net mean stress and Figure 10 shows the evolutions of shear stress and the corresponding yield stress.

In these two figures some oscillations are observed. Because of the dynamic formulation, whenever there is an unbalanced force in a node, some elastic waves are generated and cross the domain reflecting at the boundaries (if the boundaries are not

absorbing boundaries, as the case solved in the example). A sudden change of external or internal forces can be the reason of the excitation. For example, these could be related with some remaining cell crossing noise (Bardenhagen & Kober, 2004) during the motion of the slide. A sudden decrease of the stress level due to softening can also be a cause of the oscillations.

Another reason that can explain the onset of oscillations is a sudden change of the stiffness of the soil. If solid grains are incompressible, the bulk modulus of the unsaturated soil can be written as (Santamarina, 2001):

$$K_m = K_s + \frac{1}{\frac{nS_l}{K_l} + \frac{n(1-S_l)}{K_g}} \tag{42}$$

where K_s, K_l and K_g are the modulus of the solid skeleton, liquid and gas.

Figure 12 shows the variation of the unsaturated bulk modulus with the degree of saturation considering the water retention curve and the soil properties of this case. It is clear that when the soil is almost saturated and the degree of saturation is close to one, the stiffness of the soil increases abruptly towards the saturated bulk modulus. This effect can be explained because the stiffness of the gas is several orders of magnitude lower than the stiffness of water and soil skeleton. Comparing Figures 9 and 10 with Figure 8b it can be noted that these oscillations are mainly originated when the degree of saturation of the material point is close to one (saturated material).

A smoothing of results has been introduced in Figures 9 and 10 to facilitate the plot of stress paths. The superimposed plot of the available Mohr-Coulomb strength provides an additional insight into the slope behaviour. The material point S1 at the slope toe is essentially yielding at the start of the simulation (Figure 10a) and it maintains plastic conditions throughout the sliding process. Point S2, the shallow point at mid slope plastifies about 12 s after the beginning of rainfall and it remains in a plastic state. D2, which is located within the shear band, behaves essentially as S2. Point D1 at the slope toe, at a certain depth, is apparently in an elastic state throughout the sliding process although it appears to be very close to plastification at the final stages of sliding (Figure 10b).

Stress paths in a $\bar{p}$-q plane, plotted in Figure 11, offer a more precise information on the evolution of plastic states. Initially, when the wetting starts but the slope is still stable (from t_1 to t_2), the stress state for the deeper and more confined points (D1,

D2) changes slightly. However, shallower points subjected to higher shear stresses such as the toe of the slope (S1) are subjected to a faster decrease of suction and a loss of strength is associated with suction softening. S1 is under plastic conditions from the beginning of the calculation. The material point remains on the yield surface as it shrinks, due to the rapid loss of suction. The point initially experiences a decrease in net mean stress, which is later recovered as the slide "flows" over this point.

The slide motion begins between times t_2 and t_3. These points located mid-slope, in the "active" area of the failure (S2 and D2), suffer a small increase of mean and shear stresses but they remain in the current yield surface. Points located in the "passive" area experience large stress changes. The shallower S1 point softens because of the rapid reduction of suction. Beyond t_3, those points located at mid-slope (S2 and D2) maintain the stress state rather constant. Confinement increases on S1 and it is capable of offering higher shear strength. The deeper D1 point is able to resist the stress changes associated with the change in slope geometry and the overall softening of the upper part of slope. D1 remains elastic but close to the failure envelope for saturated states at the advanced stages of wetting.

6.4. Dynamics of the motion

The model provides also information on the overall dynamic behaviour of the slide. This is a significant improvement over static formulations. The calculated total displacement, velocity and acceleration of S1, S2, D1 and D2 are shown in Figure 13. Velocities and accelerations represented in Figures 13b and 13c have been calculated by applying a smoothing on the total displacements. Analyzing these plots it can be seen that the embankment remains essentially stable during the first 20 seconds after the initiation of wetting. At time t_2, the failure mechanism develops and control points located in the mobilized volume (S1, S2 and D2) start moving. They accelerate quickly during fifteen additional seconds. Peak velocity is attained at t_3 = 35 s. After a peak value, the velocity and the acceleration decrease and the slope tends to stabilize. The resting period may be divided in two parts: a fast decrease of velocity and acceleration followed by a progressive reduction of velocity towards a new state of equilibrium. This reaction cannot be generalized and it will depend strongly on the slope geometry. The lower horizontal platform contributes, in the example solved, to arrest the motion after a relatively small displacement. The

589 control point S2 moves 4 m, reaches a maximum velocity of 0.1 m/s and achieves an
590 acceleration of 9 mm/s^2. Note that the dynamic variables depend on the position of
591 the point within the slope. Establishing a slope run-out requires some conventions.
592 For instance, if it is defined as the distance between the slope toes before and after
593 failure, a run-out of 2.5 m is calculated, as mentioned before. This is a smaller value
594 than the distance travelled by the material points located at mid-slope, close to the
595 surface, but larger than other material points examined in this analysis.

596 ## 7. CONCLUSIONS

597 The paper presents a step forward in the application of MPM to multiphase
598 problems in granular media. The choice selected is to lump soil properties, stresses
599 and state variables into the material points. Three phases are necessary in an analysis
600 of unsaturated soils: gas, liquid and solid. Mass balance equations of the species (air,
601 water, minerals) as well as all constitutive relationships are formulated at a material
602 point level. Equilibrium is established in dynamic terms for the gas, the liquid and
603 the mixture. Accelerations are calculated in the computational mesh. Velocities,
604 displacements and strains are obtained into the material points. Soil properties are
605 updated and mass balance equations provide the relationships to find water and gas
606 pressures. The outlined computational cycle is an explicit marching scheme in time.
607 This approach offers numerical advantages in terms of computing time in problems
608 which do not require a physical separation (different domains) between the granular
609 skeleton and fluid phases. This is the case of the application discussed in the paper,
610 namely the instability of unsaturated slopes induced by rainfall wetting. This is a
611 relevant practical problem in virtually all climate and soil conditions. The method
612 handles in a natural way the kinematics of sliding and it provides information on
613 velocities, accelerations and run-outs, which help to estimate the expected damage in
614 case of sliding.

615 The general method, developed in some detail, has been applied to unsaturated
616 soils described by an elastoplastic suction dependent Mohr-Coulomb model
617 formulated in terms of two stress fields: net stress and suction. A simple
618 embankment slope, whose characteristics were taken from a real case involving
619 surface instability induced by heavy rains, has been analyzed. The model provides an
620 insight into the coupled flow-stress-strain mechanisms developing in the slope.

621 Suction decrease results in a marked strength softening. Deviatoric strain localization
622 starts at the slope toe and eventually materializes into a full sliding zone. The slope
623 motion starts when a shallow band of soil reaches a low (but non-zero) suction value
624 and accelerates in a few seconds. The slide does not displace as a rigid body,
625 however. Points close to the surface experience a faster and more intense suction
626 reduction and their strength reaches soon the minimum value (saturated conditions).
627 They are capable of "flowing" over the more resistant zones at depth. The end result
628 is a complex motion which makes it difficult to define run-out, velocity and
629 acceleration in a clear and simple way. In fact, these variables depend on the material
630 point position within the sliding volume. This is believed to be the case in practice
631 when observing rain-induced instabilities.
632 The MPM, as formulated in the paper, is an advanced prediction tool to
633 investigate the stability of slopes in partially saturated soils. The degree of mesh
634 dependence of the results has not been evaluated in the paper. Grid density may
635 affect the computed velocities or displacement. The focus of the paper is to develop a
636 general MPM formulation for saturated and unsaturated deformable porous media.
637 Sensitivity analyses regarding the number of material points and nodes have been left
638 outside of the scope of this paper.
639 Other large deformation problems, such as wetting induced collapse or swelling
640 may be analysed by the same method but they will require the consideration of a
641 different constitutive model. However, the general formulation of the three phase
642 approach described will remain unchanged.

643 ## 8. ACKNOWLEDGEMENTS

644 The code developed is a new version of a previously existing MPM code
645 developed at Deltares, Delft. The authors acknowledge with thanks the support
646 provided by the MPM Deltares group and by the remaining members of the MPM
647 Research Community (University of Cambridge and Technische Universität
648 Hamburg-Harburg).

649 The first author also wants to acknowledge the grant FPI provided by the Spanish
650 Ministry of Science and Innovation (MICINN).

651 REFERENCES

652 Abbo, A & Sloan, S (1995) A smooth hyperbolic approximation to the Mohr-
653 Coulomb yield criterion. *Computers & Structures* **54(3)**: 427–441.

654 Abe, K, Soga, K and Bandara, S (2014) Material point method for coupled
655 hydromechanical problems. *Journal of Geotechnical and Geoenvironmental*
656 *Engineering* **140(3)**: 1–16, doi:10.1061/(ASCE)GT.1943-5606.0001011.

657 Al-Kafaji, IKJ (2013) *Formulation of a Dynamic Material Point Method (MPM) for*
658 *Geomechanical Problems*. *PhD Thesis.* Universität Stuttgart.

659 Alonso, EE, Pinyol, NM and Puzrin, AM (2010) *Geomechanics of Failures.*
660 *Advanced Topics*. Springer, doi:10.1007/978-90-481-3538-7.

661 Alonso, EE, Pinyol, NM and Yerro, A (2014) Mathematical Modelling of Slopes.
662 *Procedia Earth and Planetary Science* **9**: 64–73,
663 doi:10.1016/j.proeps.2014.06.002.

664 Andersen, S and Andersen, L (2010) Modelling of landslides with the material-point
665 method. *Computational Geosciences* **14(1)**: 137–147.

666 Bandara, SS (2013) *Material point method to simulate large deformation problems*
667 *in fluid-saturated granular medium*. *PhD Thesis.* University of Cambridge.

668 Bardenhagen, SG and Kober, EM (2004) The generalized interpolation material
669 point method. *Computer Modeling in Engineering and Sciences* **5(6)**: 477–495,
670 doi:10.3970/cmes.2004.005.477.

671 Beuth, L (2012) *Formulation and application of a quasi-static material point*
672 *method*. *PhD Thesis.* Universität Stuttgart.

673 Beuth, L, Wieckowski, Z and Vermeer, PA (2011) Solution of quasi-static large-
674 strain problems by the material point method. *International Journal for*
675 *Numerical and Analytical Methods in Geomechanics* **35(13)**: 1451–1465,
676 doi:10.1002/nag.

677 Buzzi, O, Pedroso, DM and Giacomini, A (2008) Caveats on the Implementation of
678 the Generalized Material Point Method. *Computer Modeling in Engineering and*
679 *Sciences* **31(2)**: 85–106.

680 Coetzee, CJ, Vermeer, PA and Basson, AH (2005) The modelling of anchors using
681 the material point method. *International Journal for Numerical and Analytical*
682 *Methods in Geomechanics* **29(9)**: 879–895, doi:10.1002/nag.439.

683 Delage, P and Graham, J (1996) Mechanical behaviour of unsaturated soil:
684 understanding the behaviour of unsaturated soils requires reliable conceptual
685 models. In *Proceedings of 1st International Conference on Unsaturated soils,*
686 *Paris* (Alonso EE and Delage P (eds)). Balkema, Rotterdam, vol. 3, pp. 1223-
687 1256.

688 Edlefson, NE and Anderson, ABC (1943) Thermodynamics of soil moisture.
689 *Hilgardia* **15(2)**: 31–298.

690 Escario, V and Saez, J (1986) The shear strength of partly saturated soils.
691 *Geotechnique* **36(3)**: 453–456.

692 Fick, A (1855) V. On liquid diffusion. *The London, Edinburgh, and Dublin*
693 *Philosophical Magazine and Journal of Science* **10(63)**: 30–39,
694 doi:10.1080/14786445508641925.

695 Fredlund, DG, Morgensten, NR and Widger, RA (1978) The shear strength of
696 unsaturated soils. *Canadian Geotechnical Journal* **15(3)**: 313–321.

697 Galerkin, BG (1915) Series solution of some problems of elastic equilibrium of rods
698 and plates. *Vestnik Inzhenerov Tekhnikov* **19**: 897–908.

699 Genuchten, M Van (1980) A closed-form equation for predicting the hydraulic
700 conductivity of unsaturated soils. *Soil Science Society of America Journal* **44**:
701 892–898.

702 Han, KK, Rahardjo, H and Broms, B (1995) Effect of hysteresis on the shear strength
703 of a residual soil. In *Proceedings of the First International Conference on*
704 *Unsaturated Soils. UNSAT'95, Paris* (Alonso EE and Delage P (eds)). Balkema,
705 Rotterdam, vol. 2, pp. 499–504.

706 Hillel, D (1971) *Soil and Water-Physical Principles and Processes*. Academic Press,
707 Inc.

708 Huang, P, Zhang, X, Ma, S and Huang, X (2011) Contact algorithms for the material
709 point method in impact and penetration simulation. *International Journal for*
710 *Numerical Methods in Engineering* **85(4)**: 498–517, doi:10.1002/nme.

711 Jassim, I, Stolle, D and Vermeer, P (2013) Two-phase dynamic analysis by material
712 point method. *International Journal for Numerical and Analytical Methods in*
713 *Geomechanics* **37(15)**: 2502–2522, doi:10.1002/nag.

714 Kamojjala, K, Brannon, R, Sadeghirad, A and Guilkey, J (2013) Verification tests in
715 solid mechanics. *Engineering with Computers*, 1–21. doi:10.1007/s00366-013-
716 0342-x.

717 Mackay, D & Shiu, WY (1981) A critical review of Henry's law constants for
718 chemicals of environmental interest. *Journal of Physical and Chemical*
719 *Reference Data* **10(4)**: 1175–1199, doi:10.1063/1.555654.

720 Nairn, JA and Matsumoto, N (2009) Fracture modeling of crack propagation in wood
721 and wood composites including crack tip processes and fiber bridging
722 mechanics. In *Proceedings of the 12th International Conference on Fracture,*
723 *Ottawa, Canada*.

724 Potts, D and Gens, A (1985) A critical assessment of methods of correcting for drift
725 from the yield surface in elasto-plastic finite element analysis. *Numerical and*
726 *Analytical Methods in Geomechanics* **9**: 149–159.

727 Santamarina, JC (2001) *Soils and Waves*. Wiley.

728 Steffen, M, Wallstedt, P and Guilkey, J (2008) Examination and analysis of
729 implementation choices within the material point method (MPM). *Computer*
730 *Modeling in Engineering and Sciences* **32(2)**: 107–127.

731 Sulsky, D, Chen, Z and Schreyer, HL (1994) A particle method for history-
732 dependent materials. *Computer Methods in Applied Mechanics and Engineering*
733 **118(1–2)**: 179–196, doi:10.1016/0045-7825(94)90112-0.

734 Sulsky, D and Schreyer, HL (1996) Axisymmetric form of the material point method
735 with applications to upsetting and Taylor impact problems. *Computer Methods*
736 *in Applied Mechanics and Engineering* **139(1–4)**: 409–429, doi:10.1016/S0045-
737 7825(96)01091-2.

738 Sulsky, D, Schreyer, H, Peterson, K, Kwok, R and Coon, M (2007) Using the
739 material-point method to model sea ice dynamics. *Journal of Geophysical*
740 *Research: Oceans* **112(C2)**: 1–18. doi:10.1029/2005JC003329.

741 Tan, H and Nairn, J (2002) Hierarchical, adaptive, material point method for
742 dynamic energy release rate calculations. *Computer Methods in Applied*
743 *Mechanics and Engineering* **191(19-20)**: 2123–2137.

744 Vaunat, J, Romero, E, Marchi, C and Jommi, C (2002) Modelling of the shear
745 strength of unsaturated soils. In *Proceedings of the 3rd International conference*
746 *of Unsaturated Soils, UNSAT'02, Recife* (Jucá J, de Campos T and Marinho F
747 (eds.)). Swets & Zeitlinger, Lisse, pp. 245–251.

748 Wieckowski, Z (2013) Two-phase numerical model for soil-fluid interaction
749 problems. In *ComGeoIII*, Krakow (Pietruszczak S and Pande GN (eds.)). pp:
750 410–419.

751 Więckowski, Z (2004) The material point method in large strain engineering
752 problems. *Computer Methods in Applied Mechanics and Engineering* **193(39-**
753 **41)**: 4417–4438, doi:10.1016/j.cma.2004.01.035.

754 Więckowski, Z, Sung-Kie, Y and Jeoung-Heum, Y (1999) A particle-in-cell solution
755 to the silo discharging problem. *International Journal for Numerical Methods in*
756 *Engineering* **45(9)**: 1203–1225, doi:10.1002/(SICI)1097-
757 0207(19990730)45:9<1203::AID-NME626>3.0.CO;2-C.

758 Xikui, L and Zienkiewicz, O (1992) Multiphase flow in deforming porous media and
759 finite element solutions. *Computers & Structures* **45(2)**: 211–227.

760 Yerro, A, Alonso, E and Pinyol, N (2014) Modelling progressive failure with MPM.
761 In *Numerical Methods in Geotechnical Engineering NUMGE 2014, Delft*

762 (Hicks M, Brinkgreve RBJ and Rohe A (eds.)). Balkema, Leiden, The
763 Netherlands, vol. 1, pp: 319–323.

764 Zabala, F and Alonso, E (2010) *Modelación de problemas geotécnicos*
765 *hidromecánicos utilizando el método del punto material*. *PhD Thesis.*
766 Universitat Politècnica de Catalunya.

767 Zabala, F and Alonso, EE (2011) Progressive failure of Aznalcóllar dam using the
768 material point method. *Géotechnique* **61(9)**: 795–808, doi:10.1680/geot.9.P.134.

769

APPENDIX I: Development of mass balance equations

In this appendix, the developments of the mass balance equation for the solid, water and air are presented in detail starting from the equation (14) in the paper.

Mass balance equation of the solid component

Considering that there is no mass exchange between solid and fluid phases, the general mass balance equation (14) can be particularised for the solid component. It yields the differential equation (I.1), in which ρ_s is the solid density, n is the porosity and $\mathbf{j}_s^s$ are the solid fluxes. No external solid mass sources or sinks have been considered.

$$\frac{\partial}{\partial t}\left(\rho_s\left(1-n\right)\right)+\nabla\cdot\left(\mathbf{j}_s^s\right)=0 \tag{I.1}$$

Taking into account the solid flux equal to the advective flux of the solid (I.2), equation (I.1) yields the expression (I.3).

$$\mathbf{j}_s^s=\left(\rho_s\left(1-n\right)\right)\mathbf{v}_s \tag{I.2}$$

$$\frac{\partial}{\partial t}\left(\rho_s\left(1-n\right)\right)+\nabla\cdot\left(\rho_s\left(1-n\right)\mathbf{v}_s\right)=0 \tag{I.3}$$

Applying the chain rule for all the derivatives, the previous equation can be rewritten as:

$$\left(1-n\right)\frac{\partial\rho_s}{\partial t}+\left(1-n\right)\left(\mathbf{v}_s\cdot\nabla\rho_s\right)-\rho_s\frac{\partial n}{\partial t}-\rho_s\left(\mathbf{v}_s\cdot\nabla n\right)+\rho_s\left(1-n\right)\nabla\cdot\mathbf{v}_s=0 \tag{I.4}$$

Regrouping terms considering the definition of the material derivative (I.5), the solid mass balance is simplified to equation (I.6).

$$\frac{D_s\left(\bullet\right)}{Dt}=\frac{\partial\left(\bullet\right)}{\partial t}+\mathbf{v}_s\cdot\nabla\left(\bullet\right) \tag{I.5}$$

$$\left(1-n\right)\frac{D_s\rho_s}{Dt}-\rho_s\frac{D_s n}{Dt}+\rho_s\left(1-n\right)\nabla\cdot\mathbf{v}_s=0 \tag{I.6}$$

Rearranging terms, the following expression is obtained:

$$\frac{D_s n}{Dt}=\frac{\left(1-n\right)}{\rho_s}\frac{D\rho_s}{Dt}+\left(1-n\right)\nabla\cdot\mathbf{v}_s \tag{I.7}$$

Finally, considering that the solid grains are incompressible, the material derivative of the porosity is derived as:

$$\frac{D_s n}{Dt}=\left(1-n\right)\nabla\cdot\mathbf{v}_s \tag{I.8}$$

Mass balance equation of the water component

Taking into account that exchange of water mass is allowed between the fluid phases, the water mass balance equation should include the water content within both

liquid and gas phases. Starting from equation (14), the mass balance equation for water, without considering external sources or sinks, can be written as:

$$\frac{\partial}{\partial t}\left(\omega_g^w \rho_g S_g n + \omega_l^w \rho_l S_l n\right) + \nabla \cdot \left(\mathbf{j}_g^w + \mathbf{j}_l^w\right) = 0 \tag{I.9}$$

where ρ_g and ρ_l are the gas and liquid densities; S_g and S_l are the gas and liquid degree of saturations (S_g =1- S_l); ω_g^w and ω_l^w are the mass fractions of water in the gas and in the liquid respectively; and $\mathbf{j}_g^w$ and $\mathbf{j}_l^w$ are the fluxes of water in the gas and in the liquid phases.

Referring to the water fluxes, the flux in the gas phase (I.10) is equal to the sum of a diffusive term $\mathbf{i}_g^w$ and an advective term. On the other hand, the water flux in the liquid phase can be written as (I.11), in which the diffusive term has been neglected.

$$\mathbf{j}_g^w = \mathbf{i}_g^w + \left(\omega_g^w \rho_g S_g n\right)\mathbf{v}_g \tag{I.10}$$

$$\mathbf{j}_l^w = \left(\omega_l^w \rho_l S_l n\right)\mathbf{v}_l \tag{I.11}$$

Substituting equations (I.10) and (I.11) in (I.9), the water mass balance can be written as follows:

$$\frac{\partial}{\partial t}\left(\omega_g^w \rho_g S_g n + \omega_l^w \rho_l S_l n\right) + \nabla \cdot \left(\omega_g^w \rho_g S_g n \mathbf{v}_g\right) + \nabla \cdot \left(\omega_l^w \rho_l S_l n \mathbf{v}_l\right) + \nabla \cdot \mathbf{i}_g^w = 0 \tag{I.12}$$

Regrouping terms considering the definition of liquid and gas material derivative, (I.13) and (I.14) respectively, the water mass balance is rewritten in (I.15).

$$\frac{D_l(\bullet)}{Dt} = \frac{\partial(\bullet)}{\partial t} + \mathbf{v}_l \cdot \nabla(\bullet) \tag{I.13}$$

$$\frac{D_g(\bullet)}{Dt} = \frac{\partial(\bullet)}{\partial t} + \mathbf{v}_g \cdot \nabla(\bullet) \tag{I.14}$$

$$\begin{aligned}&\left(\omega_g^w \rho_g S_g\right)\frac{D_g n}{Dt} + \left(\omega_l^w \rho_l S_l\right)\frac{D_l n}{Dt} + n\frac{D_g\left(\omega_g^w \rho_g S_g\right)}{Dt} + n\frac{D_l\left(\omega_l^w \rho_l S_l\right)}{Dt} + \\ &+ n\left(\omega_g^w \rho_g S_g\right)\nabla \cdot \mathbf{v}_g + n\left(\omega_l^w \rho_l S_l\right)\nabla \cdot \mathbf{v}_l + \nabla \cdot \mathbf{i}_g^w = 0\end{aligned} \tag{I.15}$$

Assuming the distribution of porosity is sufficiently smooth and the spatial variations of water content in the liquid and in the gas are small, the material derivatives of (I.15) can be simplified according to (I.16).

$$\frac{D_s(\bullet)}{Dt} \approx \frac{D_l(\bullet)}{Dt} \approx \frac{D_g(\bullet)}{Dt} \approx \frac{D(\bullet)}{Dt} \tag{I.16}$$

Considering the previous assumptions and including equation (I.8) in (I.15), the water mass balance equation can be rewritten as:

$$\begin{aligned}&n\frac{D\left(\omega_g^w \rho_g S_g + \omega_l^w \rho_l S_l\right)}{Dt} = \\ &= -(1-n)\left(\omega_g^w \rho_g S_g + \omega_l^w \rho_l S_l\right)\nabla \cdot \mathbf{v}_s - n\left(\omega_g^w \rho_g S_g\right)\nabla \cdot \mathbf{v}_g - n\left(\omega_l^w \rho_l S_l\right)\nabla \cdot \mathbf{v}_l - \nabla \cdot \mathbf{i}_g^w\end{aligned} \tag{I.17}$$

Finally, taking into account the liquid pressure and the gas pressure (p_l and p_g) as state variables of the equation, the time derivative of equation (I.17) can be expanded as follows:

$$\frac{D\left(\omega_g^w \rho_g S_g + \omega_l^w \rho_l S_l\right)}{Dt} = \frac{D\left(\omega_g^w \rho_g S_g + \omega_l^w \rho_l S_l\right)}{Dp_l}\dot{p}_l + \frac{D\left(\omega_g^w \rho_g S_g + \omega_l^w \rho_l S_l\right)}{Dp_g}\dot{p}_g \qquad \text{(I.18)}$$

where the dot on p_l and p_g indicates the variation in time of liquid and gas pressure.

In the calculation, the mass fraction of the water in the liquid, ω_l^w, is assumed equal to one.

Mass balance equation of the air component

Similarly to what has been done with the water mass balance equation, the air mass balance equation has been developed considering air content in the two fluid phases. Starting from equation (14), the air mass balance, without considering external sources or sinks, can be written as:

$$\frac{\partial}{\partial t}\left(\omega_l^a \rho_l S_l n + \omega_g^a \rho_g S_g n\right) + \nabla \cdot \left(\mathbf{j}_l^a + \mathbf{j}_g^a\right) = 0 \qquad \text{(I.19)}$$

where $\mathbf{j}_g^a$ and $\mathbf{j}_l^a$ are the fluxes of air in the gas and liquid phases. The air flux in the liquid phase (I.20) is equal to the sum of the diffusive term $\mathbf{i}_l^a$ and the advective term. The air flux in the gas phase can be written as (I.21), in which the diffusive term is be neglected.

$$\mathbf{j}_l^a = \mathbf{i}_l^a + \left(\omega_l^a \rho_l S_l n\right)\mathbf{v}_l \qquad \text{(I.20)}$$

$$\mathbf{j}_g^a = \left(\omega_g^a \rho_g S_g n\right)\mathbf{v}_g \qquad \text{(I.21)}$$

Substituting equations (I.20) and (I.21) in the (I.19) and arranging terms, the water mass balance can be written with the following expression:

$$\frac{\partial}{\partial t}\left(\omega_l^a \rho_l S_l n + \omega_g^a \rho_g S_g n\right) + \nabla \cdot \left(\omega_l^a \rho_l S_l n \mathbf{v}_l\right) + \nabla \cdot \left(\omega_g^a \rho_g S_g n \mathbf{v}_g\right) + \nabla \cdot \mathbf{i}_g^a = 0 \qquad \text{(I.22)}$$

Regrouping terms considering the definition of liquid and gas material derivative, (I.13) and (I.14) respectively, the air mass balance is rewritten in (I.23).

$$\begin{aligned}&\left(\omega_l^a \rho_l S_l\right)\frac{D_l n}{Dt} + \left(\omega_g^a \rho_g S_g\right)\frac{D_g n}{Dt} + n\frac{D_l\left(\omega_l^a \rho_l S_l\right)}{Dt} + n\frac{D_g\left(\omega_g^a \rho_g S_g\right)}{Dt} + \\ &+ n\left(\omega_l^a \rho_l S_l\right)\nabla \cdot \mathbf{v}_l + n\left(\omega_g^a \rho_g S_g\right)\nabla \cdot \mathbf{v}_g + \nabla \cdot \mathbf{i}_g^a = 0\end{aligned} \qquad \text{(I.23)}$$

Assuming the distribution of porosity is sufficiently smooth and the spatial variations of air content in the liquid and in the gas are small, the material derivatives of (I.23) can be simplified according to (I.16). Considering these assumptions and including equation (I.8) in (I.23), the air mass balance equation can be rewritten as:

856
$$n\frac{D\left(\omega_l^a \rho_l S_l + \omega_g^a \rho_g S_g\right)}{Dt} = \\ = -(1-n)\left(\omega_l^a \rho_l S_l + \omega_g^a \rho_g S_g\right)\nabla \cdot \mathbf{v}_s - n\left(\omega_l^a \rho_l S_l\right)\nabla \cdot \mathbf{v}_l - n\left(\omega_g^a \rho_g S_g\right)\nabla \cdot \mathbf{v}_g - \nabla \cdot \mathbf{i}_g^a \quad \text{(I.24)}$$

857 Finally, taking into account the liquid pressure and the gas pressure (p_l and p_g) as
858 state variables of the equation, the time derivative of (I.24) can be expanded as
859 follows:

860
$$\frac{D\left(\omega_l^a \rho_l S_l + \omega_g^a \rho_g S_g\right)}{Dt} = \frac{D\left(\omega_l^a \rho_l S_l + \omega_g^a \rho_g S_g\right)}{Dp_l}\dot{p}_l + \frac{D\left(\omega_l^a \rho_l S_l + \omega_g^a \rho_g S_g\right)}{Dp_g}\dot{p}_g \quad \text{(I.25)}$$

861 In the calculation, the mass fraction of the air in the gas, ω_g^a, is assumed equal to one.

862

APPENDIX II: Development the momentum balance equations

In this appendix, the strong forms (differential equation) of the momentum balance equations for liquid (11), gas (12) and mixture (13), are transformed to the weak forms (integral equation) using weighted residuals. Then the momentum balance equations are discretized considering the two MPM frames already described in the paper: nodes and material points.

Weak form of the momentum balance equation of fluid phases

Momentum balance equation is solved in a boundary value problem for the two fluid phases. To avoid the repetition of similar equations, in the following, the subscript "*f*" indicates the phase that corresponding to liquid and gas. Notice that "*s*" remains to indicate the solid phase.
Equation (II.1a) is the strong form of momentum balance equation and (II.1b) and (II.1c) are the corresponding displacement and pressure boundary conditions.

$$\rho_f \mathbf{a}_f = \nabla p_f - \frac{nS_f \mu_f}{k_f}\left(\mathbf{v}_f - \mathbf{v}_s\right) + \rho_f \mathbf{b} \tag{II.1a}$$

$$\mathbf{u}_f\left(\mathbf{x},t\right) = \hat{\mathbf{u}}_f\left(t\right) \qquad \text{on} \quad \partial\Omega^{u_f} \tag{II.1b}$$

$$p_f\left(\mathbf{x},t\right)\mathbf{n} = \hat{\mathbf{p}}_f\left(t\right) \qquad \text{on} \quad \partial\Omega^{p_f} \tag{II.1c}$$

The weak form is derived by multiplying (II.1) by a test function $\delta\mathbf{u}_f$ and integrating over the total domain Ω. In addition, the integration by parts and the divergence theorem are applied to the term with the fluid pressure gradient. Considering that any test function can be selected, in particular one that is zero on the boundary where displacements are prescribed, the momentum balance of a fluid can be written as:

$$\begin{aligned}\int_\Omega \rho_f \delta\mathbf{u}_f \cdot \mathbf{a}_f d\Omega = \int_{\partial\Omega^{p_f}} \delta\mathbf{u}_f \cdot \hat{\mathbf{p}}_f d\partial\Omega^{p_f} - \int_\Omega \left(\nabla\cdot\delta\mathbf{u}_f\right) p_f d\Omega - \\ - \int_\Omega \frac{nS_f\mu_f}{k_f}\delta\mathbf{u}_f\cdot\left(\mathbf{v}_f - \mathbf{v}_s\right)d\Omega + \int_\Omega \rho_f \delta\mathbf{u}_f\cdot\mathbf{b}d\Omega\end{aligned} \tag{II.2}$$

where $\partial\Omega^{pf}$ is the boundary where the fluid pressure is prescribed.
Taking into account equation (37) of the manuscript (particularized for the test function $\delta\mathbf{u}_f$, fluid velocity $\mathbf{v}_f$, solid velocity $\mathbf{v}_s$ and fluid acceleration $\mathbf{a}_f$) the integral form (II.2) can be discretized to the nodes. Using the subscripts *i* and *j* to denote the nodal variables, the equation results in the following expression:

$$\begin{aligned}\sum_{i=1}^{Nn}\delta\mathbf{u}_{f_j}\cdot\sum_{j=1}^{Nn}\int_\Omega \rho_f N_i N_j \mathbf{a}_{f_j} d\Omega = \sum_{i=1}^{Nn}\delta\mathbf{u}_{f_j}\cdot\int_{\partial\Omega^{p_f}} N_i\hat{\mathbf{p}}_f d\partial\Omega^{p_f} - \sum_{i=1}^{Nn}\delta\mathbf{u}_{f_j}\cdot\int_\Omega\left(\nabla N_i\right)\cdot p_f\mathbf{m}d\Omega - \\ - \sum_{i=1}^{Nn}\delta\mathbf{u}_{f_j}\cdot\sum_{j=1}^{Nn}\int_\Omega\frac{nS_f\mu_f}{k_f}N_i N_j\left(\mathbf{v}_{f_j}-\mathbf{v}_{s_j}\right)d\Omega + \sum_{i=1}^{Nn}\delta\mathbf{u}_{f_j}\cdot\int_\Omega\rho_f N_i\mathbf{b}d\Omega\end{aligned} \tag{II.3}$$

where N_i is the shape function associated to the node *i*.
Because the components of the test function are arbitrary except at constrained boundary nodes where the components of displacement are prescribed, the previous

scalar equation can be expanded into a system of equations. Rearranging terms, it can be shown that:

$$\sum_{j=1}^{Nn}\left(\int_{\Omega}\rho_f N_i N_j d\Omega\right)\mathbf{a}_{f\,j} = \int_{\partial\Omega^{p_f}} N_i\hat{\mathbf{p}}_f d\partial\Omega^{p_f} - \int_{\Omega}\left(\nabla N_i\right)\cdot p_f\mathbf{m}d\Omega - \\ -\sum_{j=1}^{Nn}\left(\int_{\Omega}\frac{nS_f\mu_f}{k_f}N_i N_j d\Omega\right)\left(\mathbf{v}_{f\,j}-\mathbf{v}_{s\,j}\right)+\int_{\Omega}\rho_f N_i\mathbf{b}d\Omega \tag{II.4}$$

Finally, the spatial discretization is further carried out with the introduction of equation (33) of the manuscript. It is equivalent to consider a quadrature over the material points, in which the integrals are approximated by sums. The subscripts or superscript *p* is used to denote material point variable.

$$\sum_{j=1}^{Nn}\left(\sum_{p=1}^{Np}\tilde{m}_f^p N_i^p N_i^p\right)\mathbf{a}_{f\,j} = \int_{\partial\Omega^{p_f}} N_i^p\hat{\mathbf{p}}_f d\partial\Omega^{p_f} - \sum_{p=1}^{Np}\left(\nabla N_i^p\right)\cdot p_f\mathbf{m}V_p - \\ -\sum_{j=1}^{Nn}\left(\sum_{p=1}^{Np}\frac{nS_f\mu_f}{k_f}N_i^p N_i^p V_p\right)\left(\mathbf{v}_{f\,j}-\mathbf{v}_{s\,j}\right)+\sum_{p=1}^{Np}\tilde{m}_f^p N_i^p\mathbf{b} \tag{II.5}$$

In the previous equation V_p corresponds to the volume of the material point *p*, and N_i^p is the shape function of the node *i* evaluated on the corresponding material point location.

Weak form of the momentum balance equation of the mixture

The boundary value problem for the momentum balance of the mixture is the following, being (II.6a) the strong form of the equation and (II.6b) and (II.6c) the corresponding displacement and pressure boundary conditions.

$$\rho_s(1-n)\mathbf{a}_s + \rho_l nS_l\mathbf{a}_l + \rho_g nS_g\mathbf{a}_g = \nabla\cdot\boldsymbol{\sigma} + \rho_m\mathbf{b} \tag{II.6a}$$

$$\mathbf{u}_s(\mathbf{x},t) = \hat{\mathbf{u}}_s(t) \qquad \text{on} \quad \partial\Omega^{u_s} \tag{II.6b}$$

$$\boldsymbol{\sigma}(\mathbf{x},t)\cdot\mathbf{n} = \hat{\mathbf{t}}(t) \qquad \text{on} \quad \partial\Omega^{t} \tag{II.6c}$$

The weak form is derived by multiplying (II.6a) by a test function $\delta\mathbf{u}$ and integrating over the total domain Ω. In addition, the integration by parts and the divergence theorem are applied to the term with the total stress gradient. Since test functions are arbitrary, in particular one that is zero on the boundary where displacements are prescribed, the above equation can be written as:

$$\int_{\Omega}\rho_s(1-n)\delta\mathbf{u}\cdot\mathbf{a}_s d\Omega + \int_{\Omega}\rho_l nS_l\delta\mathbf{u}\cdot\mathbf{a}_l d\Omega + \int_{\Omega}\rho_g nS_g\delta\mathbf{u}\cdot\mathbf{a}_g d\Omega = \\ = \int_{\partial\Omega^t}\delta\mathbf{u}\cdot\hat{\mathbf{t}}d\partial\Omega^t - \int_{\Omega}\left(\nabla\cdot\delta\mathbf{u}\right)\cdot\boldsymbol{\sigma}d\Omega + \int_{\Omega}\rho_m\delta\mathbf{u}\cdot\mathbf{b}d\Omega \tag{II.7}$$

where $\partial\Omega^t$ is the boundary where the external traction is prescribed.
Considering equation (37) of the manuscript (particularized for the test function $\delta\mathbf{u}$, solid acceleration $\mathbf{v}_s$, liquid acceleration $\mathbf{a}_l$ and gas acceleration $\mathbf{a}_g$) the integral form (II.7) is discretized to the nodes. The equation results in the following expression:

$$\sum_{i=1}^{Nn}\delta\mathbf{u}_i\cdot\sum_{j=1}^{Nn}\int_\Omega\rho_s(1-n)N_i^pN_j^p\mathbf{a}_{s\,j}d\Omega+\sum_{i=1}^{Nn}\delta\mathbf{u}_i\cdot\sum_{j=1}^{Nn}\int_\Omega\rho_l nS_lN_i^pN_j^p\mathbf{a}_{l\,j}d\Omega+\sum_{i=1}^{Nn}\delta\mathbf{u}_i\cdot\sum_{j=1}^{Nn}\int_\Omega\rho_g nS_gN_i^pN_j^p\mathbf{a}_{g\,j}d\Omega=$$
$$\sum_{i=1}^{Nn}\delta\mathbf{u}_i\cdot\int_{\partial\Omega^t}N_i^p\hat{\mathbf{t}}d\partial\Omega^t-\sum_{i=1}^{Nn}\delta\mathbf{u}_i\cdot\int_\Omega\left(\nabla N_i^p\right)\cdot\boldsymbol{\sigma}d\Omega+\sum_{i=1}^{Nn}\delta\mathbf{u}_i\cdot\int_\Omega\rho_mN_i^p\mathbf{b}d\Omega \tag{II.8}$$

Because the components of the test function are arbitrary except at constrained boundary nodes where the components of displacement are prescribed, the previous scalar equation can be expanded into a system of equations. Rearranging terms, it can be shown that:

$$\sum_{j=1}^{Nn}\left(\int_\Omega\rho_s(1-n)N_iN_jd\Omega\right)\mathbf{a}_{s\,j}+\sum_{j=1}^{Nn}\left(\int_\Omega\rho_lnS_lN_iN_jd\Omega\right)\mathbf{a}_{l\,j}+\sum_{j=1}^{Nn}\left(\int_\Omega\rho_gnS_gN_iN_jd\Omega\right)\mathbf{a}_{g\,j}=$$
$$\int_{\partial\Omega^t}N_i\hat{\mathbf{t}}d\partial\Omega^t-\int_\Omega\left(\nabla N_i\right)\cdot\boldsymbol{\sigma}d\Omega+\int_\Omega\rho_mN_i\mathbf{b}d\Omega \tag{II.9}$$

Finally, the spatial discretization is further carried out with the consideration of equations (32) and (34). It is equivalent to consider a quadrature over the material points, in which the integrals are approximated by sums.

$$\sum_{j=1}^{Nn}\left(\sum_{p=1}^{Np}m_s^pN_i^pN_j^p\right)\mathbf{a}_{s\,j}+\sum_{j=1}^{Nn}\left(\sum_{p=1}^{Np}m_l^pN_i^pN_j^p\right)\mathbf{a}_{l\,j}+\sum_{j=1}^{Nn}\left(\sum_{p=1}^{Np}m_g^pN_i^pN_j^p\right)\mathbf{a}_{g\,j}=$$
$$\int_{\partial\Omega^t}N_i^p\hat{\mathbf{t}}\mathrm{d}\partial\Omega^t-\sum_{p}^{Np}\left(\nabla N_i^p\right)\cdot\boldsymbol{\sigma}_pV_p+\sum_{p}^{Np}m_pN_i^p\mathbf{b} \tag{II.10}$$

Final system of momentum balance equations

The discrete momentum balance equations obtained in the previous developments for the fluid phases (II.5) and for the mixture (II.10) can be written, in the same order, in a more compact form as follows:

$$\widetilde{\mathbf{M}}_\mathbf{l}\cdot\mathbf{a}_\mathbf{l}=\mathbf{F}_\mathbf{l}^\mathbf{ext}-\mathbf{F}_\mathbf{l}^\mathbf{int}-\mathbf{Q}_\mathbf{l}\cdot\left(\mathbf{v}_\mathbf{l}-\mathbf{v}_\mathbf{s}\right) \tag{II.11}$$

$$\widetilde{\mathbf{M}}_\mathbf{g}\cdot\mathbf{a}_\mathbf{g}=\mathbf{F}_\mathbf{g}^\mathbf{ext}-\mathbf{F}_\mathbf{g}^\mathbf{int}-\mathbf{Q}_\mathbf{g}\cdot\left(\mathbf{v}_\mathbf{g}-\mathbf{v}_\mathbf{s}\right) \tag{II.12}$$

$$\mathbf{M}_\mathbf{s}\cdot\mathbf{a}_\mathbf{s}+\mathbf{M}_\mathbf{l}\cdot\mathbf{a}_\mathbf{l}+\mathbf{M}_\mathbf{g}\cdot\mathbf{a}_\mathbf{g}=\mathbf{F}^\mathbf{ext}-\mathbf{F}^\mathbf{int} \tag{II.13}$$

where $\mathbf{a_s}$, $\mathbf{a_l}$, and $\mathbf{a_g}$ are the nodal acceleration vectors for the solid, liquid and gas; $\mathbf{v_s}$, $\mathbf{v_l}$, and $\mathbf{v_g}$ are the nodal velocity vectors of each phase; $\widetilde{\mathbf{M}}_\mathbf{l}$ is the liquid mass matrix per unit of liquid volume; $\widetilde{\mathbf{M}}_\mathbf{g}$ is the gas mass matrix per unit of gas volume; $\mathbf{M_s}$, $\mathbf{M_l}$ and $\mathbf{M_g}$ are the solid, liquid and gas mass matrices per unit of total volume; $\mathbf{F_l^{ext}}$, $\mathbf{F_g^{ext}}$ and $\mathbf{F^{ext}}$ are the external forces of the liquid, gas and mixture; $\mathbf{F_l^{int}}$, $\mathbf{F_g^{int}}$ and $\mathbf{F^{int}}$ are the internal forces of the liquid, gas and mixture; $\mathbf{Q_l}$ and $\mathbf{Q_g}$ are the liquid and gas dragging matrixes. The mathematical expression for each term is the following:

$$\widetilde{\mathbf{M}}_\mathbf{l}=\sum_{p}^{Np}\mathbf{N}^T\cdot\tilde{m}_l^p\mathbf{N} \tag{II.14}$$

$$\tilde{\mathbf{M}}_{\mathbf{g}} = \sum_{p}^{Np} \mathbf{N}^T \cdot \tilde{m}_g^p \mathbf{N} \tag{II.15}$$

$$\mathbf{M}_{\mathbf{l}} = \sum_{p}^{Np} \mathbf{N}^T \cdot m_l^p \mathbf{N} \tag{II.16}$$

$$\mathbf{M}_{\mathbf{g}} = \sum_{p}^{Np} \mathbf{N}^T \cdot m_g^p \mathbf{N} \tag{II.17}$$

$$\mathbf{M}_{\mathbf{s}} = \sum_{p}^{Np} \mathbf{N}^T \cdot m_s^p \mathbf{N} \tag{II.18}$$

$$\mathbf{Q}_{\mathbf{l}} = \sum_{p}^{Np} \mathbf{N}^T \cdot \frac{nS_l \mu_l}{k_l} \mathbf{N} V_p \tag{II.19}$$

$$\mathbf{Q}_{\mathbf{g}} = \sum_{p}^{Np} \mathbf{N}^T \cdot \frac{nS_g \mu_g}{k_g} \mathbf{N} V_p \tag{II.20}$$

$$\mathbf{F}_{\mathbf{l}}^{\mathbf{ext}} = \int_{\partial\Omega^{p_l}} \mathbf{N}^T \cdot \hat{\mathbf{p}}_l d\partial\Omega^{p_l} \Big|_p + \sum_{p}^{Np} \mathbf{N}^T \cdot \tilde{m}_l^p \mathbf{b} \tag{II.21}$$

$$\mathbf{F}_{\mathbf{g}}^{\mathbf{ext}} = \int_{\partial\Omega^{p_g}} \mathbf{N}^T \cdot \hat{\mathbf{p}}_g \mathbf{I} d\partial\Omega^{p_g} \Big|_p + \sum_{p}^{Np} \mathbf{N}^T \cdot \tilde{m}_g^p \mathbf{b} \tag{II.22}$$

$$\mathbf{F}^{\mathbf{ext}} = \int_{\partial\Omega^{t}} \mathbf{N}^T \cdot \hat{\mathbf{t}} d\partial\Omega^{t} \Big|_p + \sum_{p}^{Np} \mathbf{N}^T \cdot m_m^p \mathbf{b} \tag{II.23}$$

$$\mathbf{F}_{\mathbf{l}}^{\mathbf{int}} = \sum_{p}^{Np} \mathbf{B}^T \cdot p_l^p \mathbf{I} V_p \tag{II.24}$$

$$\mathbf{F}_{\mathbf{g}}^{\mathbf{int}} = \sum_{p}^{Np} \mathbf{B}^T \cdot p_g^p \mathbf{I} V_p \tag{II.25}$$

$$\mathbf{F}^{\mathbf{int}} = \sum_{p}^{Np} \mathbf{B}^T \cdot \boldsymbol{\sigma}^p V_p \tag{II.26}$$

The mass matrices written above are consistent-mass matrices. For the numerical implementation the lumped-mass matrices, which are diagonal, are used instead of the previous ones. **N** and **B** are the matrixes that contain the nodal shape functions and its gradients respectively.

966 LIST OF TABLES

967 Table 1. Numerical parameters.

Element type	Tetrahedron	
Number of elements	3654	
Number of material points	7593	
Damping factor α	0.05	
Time step	$2 \cdot 10^{-4}$	s

968 Table 2. General characteristics of the soil.

Solid density ρ_s	2700	kg/m^3
Porosity n	0.35	
Poisson ratio ν	0.33	
Liquid density ρ_l	1000	kg/m^3
Gas density ρ_g	1	kg/m^3
Liquid bulk modulus K_l	100	MPa
Gas bulk modulus K_g	0.01	MPa
Liquid viscosity μ_l	10^{-3}	kg/m·s
Gas viscosity μ_g	10^{-6}	kg/m·s
Intrinsic permeability liquid k_l	10^{-10}	m^2
Intrinsic permeability gas k_g	10^{-11}	m^2

969 Table 3. Constitutive model parameters. Suction dependent Mohr-Coulomb

Young modulus E	10	MPa
Cohesion c'	1	kPa
Friction angle φ'	20	º
Δc_{max}	15	kPa
B	0.07	
A	0.01	

970 Table 4. Retention curve parameters.

S_{min}	0	
S_{max}	1	
P_0	50	kPa
λ	0.09	

971

972

973 LIST OF FIGURES

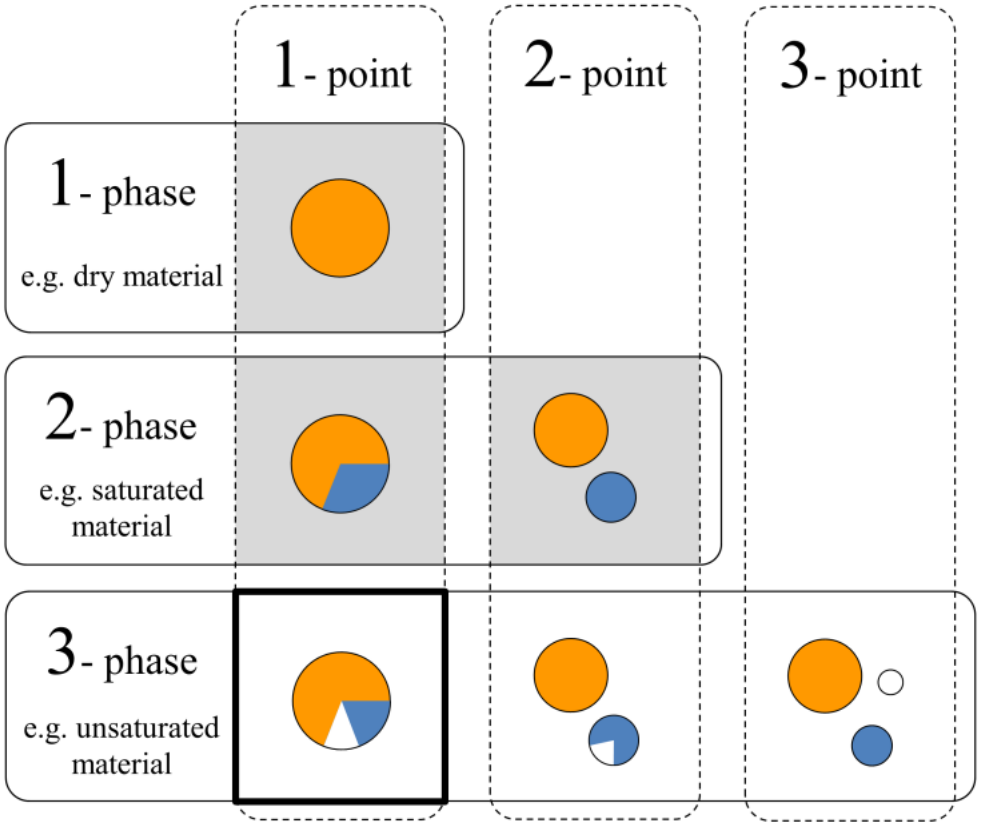

974

975 Figure 1. Scheme of the different MPM numerical approaches depending on the
976 number of phases and the number of material point sets.

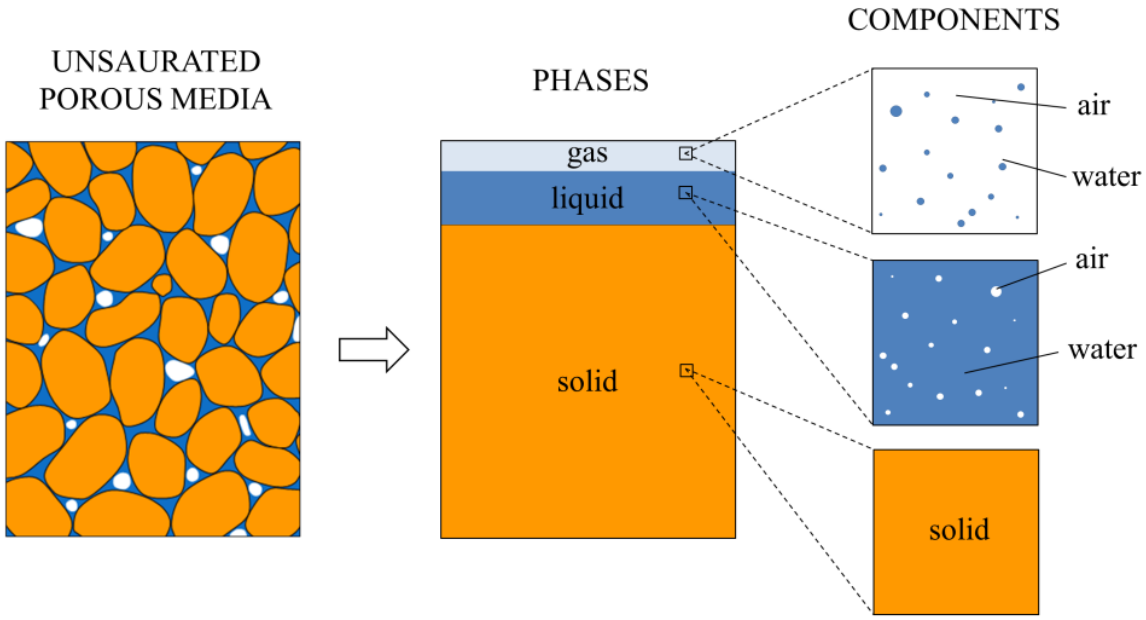

977
978 Figure 2. Continuum approximation of unsaturated porous media.

979

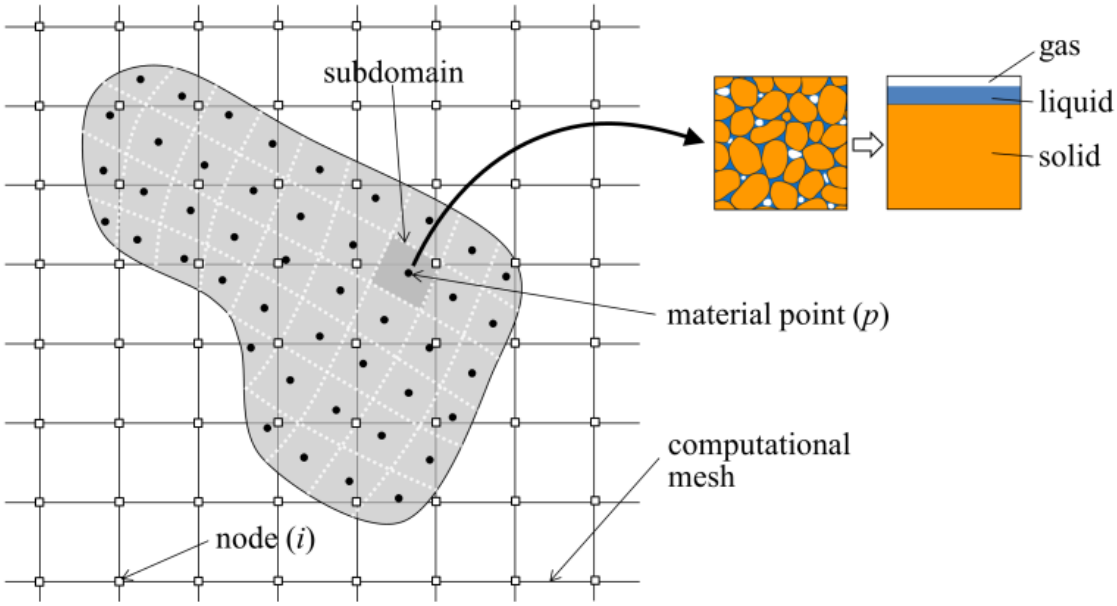

Figure 3. Scheme of the spatial discretizations of the domain.

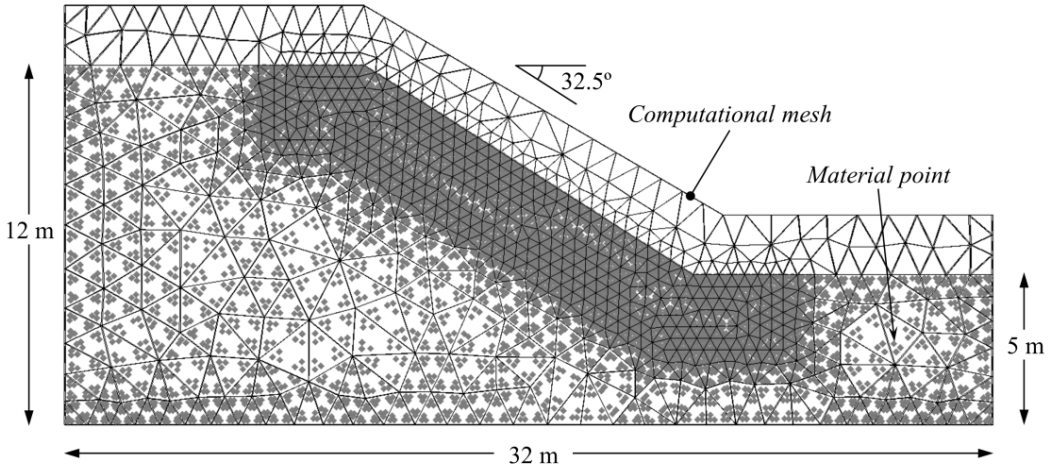

Figure 4. Geometry of the embankment slope, computational mesh and initial distribution of the material points.

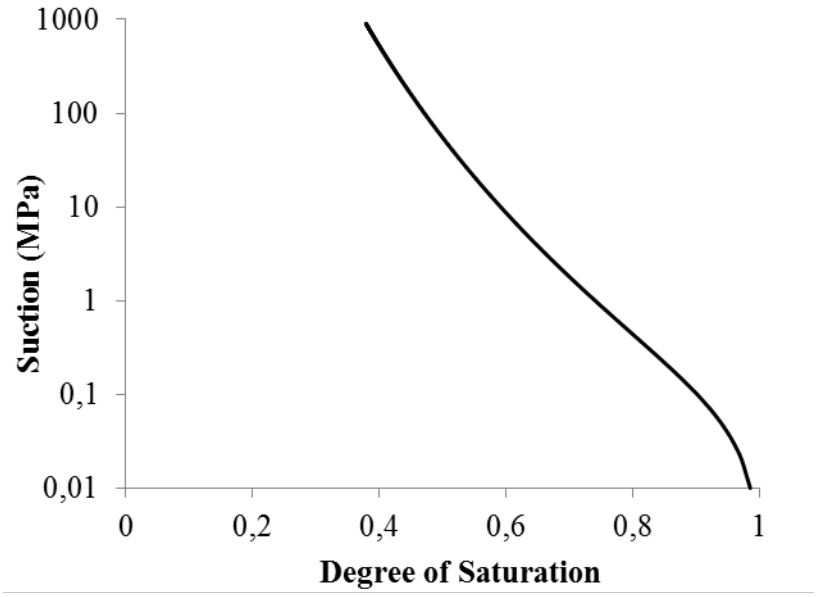

990

991 Figure 5. Water retention curve considered for the calculation.

992

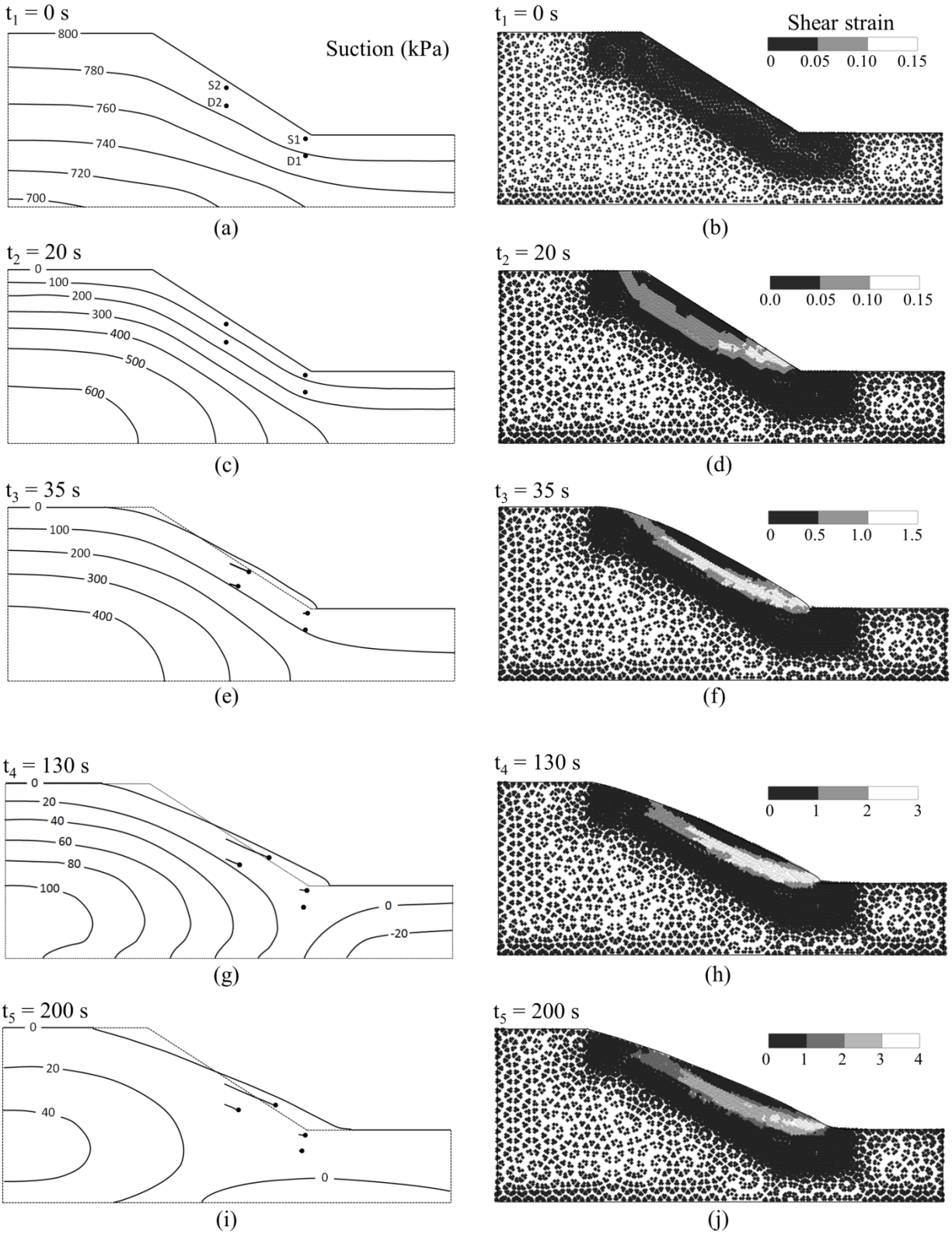

Figure 6. Calculated suction and equivalent shear strain contours at 5 different times (t_1, t_2, t_3, t_4 and t_5). The paths of 4 control material points (S1, S2, D1 and D2) are indicated.

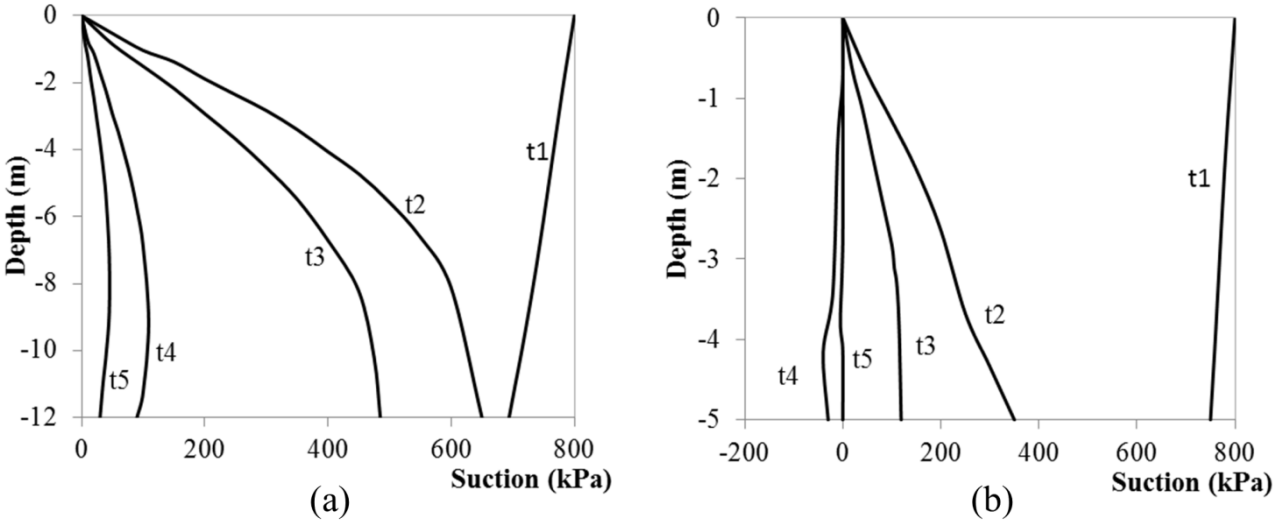

Figure 7. Suction evolution green field at 5 different times: (a) left boundary and (b) right boundary.

1002

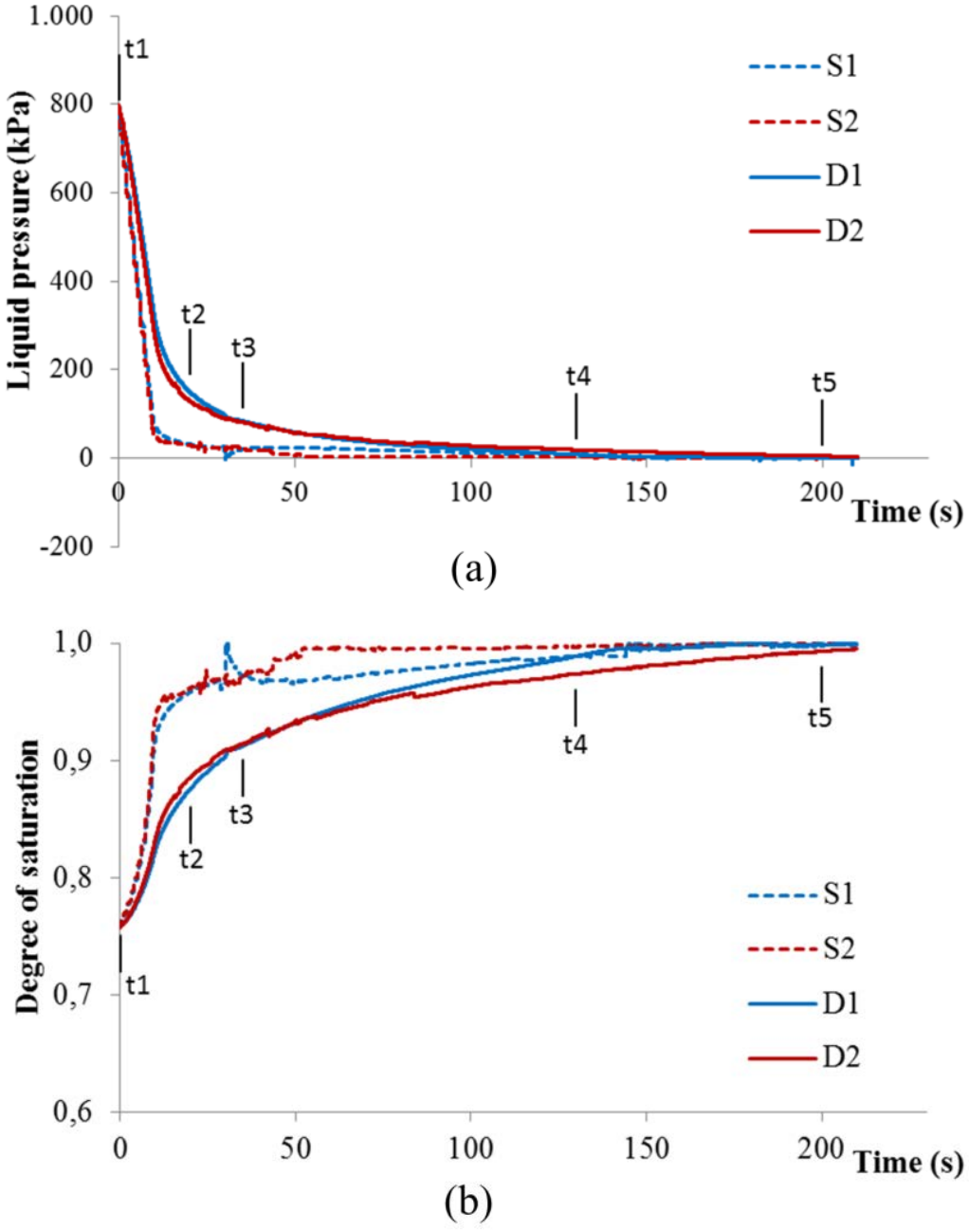

1003 Figure 8. Evolution of (a) liquid pressure and (b) degree of saturation evolution of
1004 material points S1, S2, D1, D2.

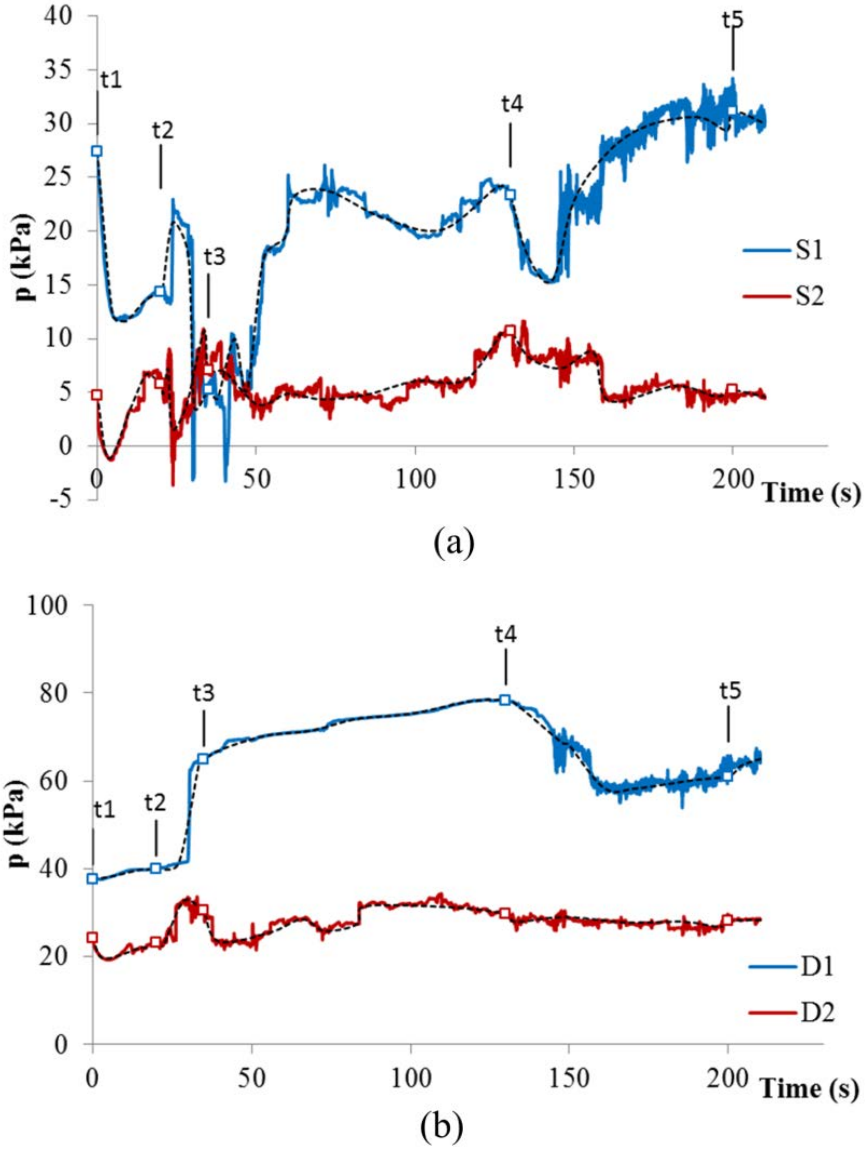

1005

1006

1007 Figure 9. Calculated net mean stress evolution of (a) shallow points (S1, S2) and (b)
1008 deep points (D1, D2).

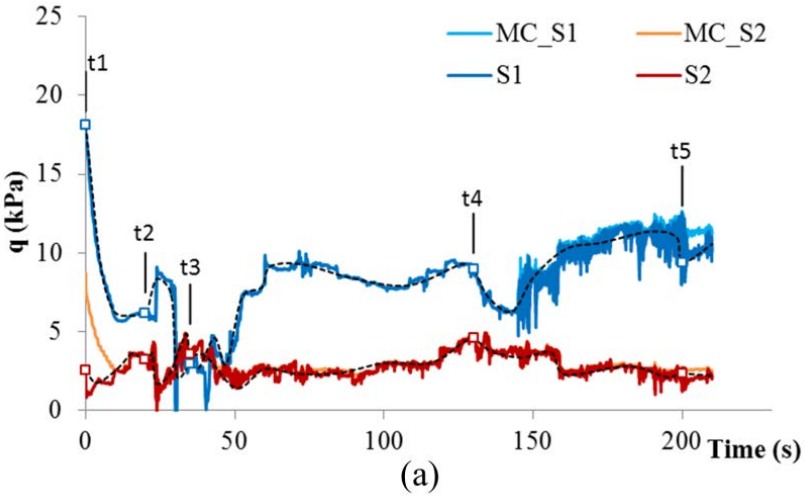

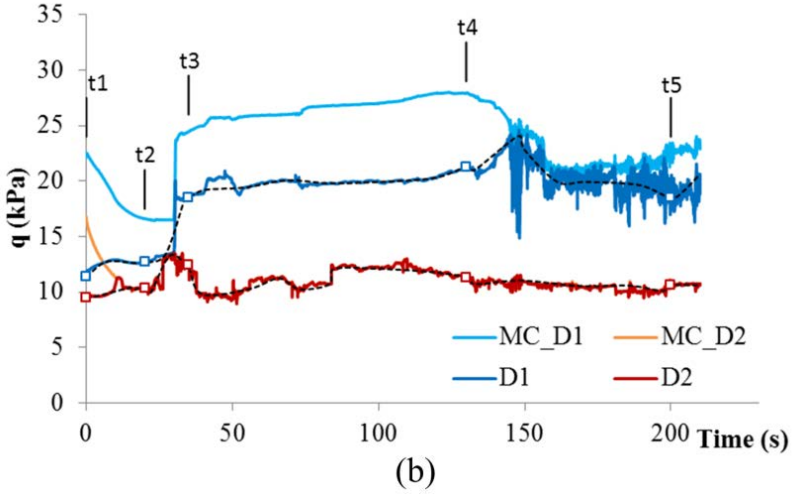

Figure 10. Calculated shear stress evolution of (a) shallow control points (S1, S2) and (b) deep control points (D1, D2). Evolution of Mohr-Coulomb (MC) yield shear stress is also indicated for each point.

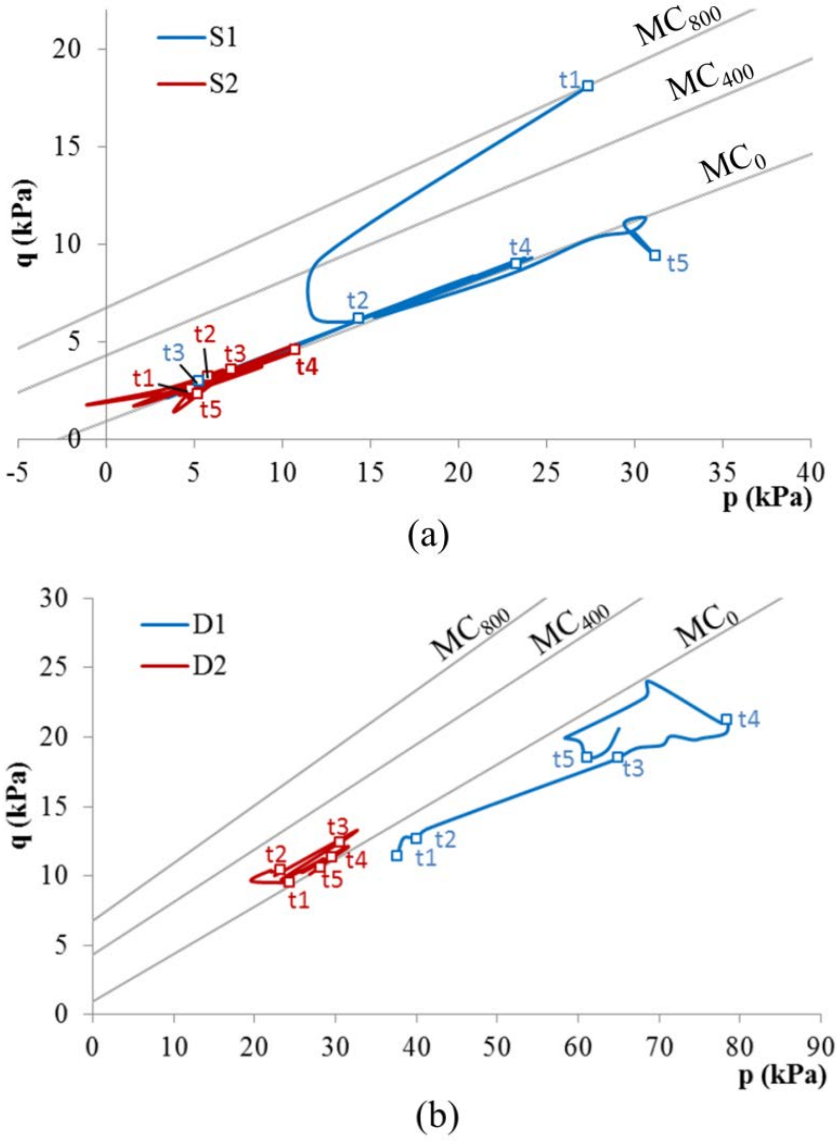

Figure 11. Stress paths of (a) shallow points (S1, S2) and (b) deep points (D1, D2). Mohr-Coulomb criterion is represented for three different suctions (800 kPa, 400 kPa and 0 kPa).

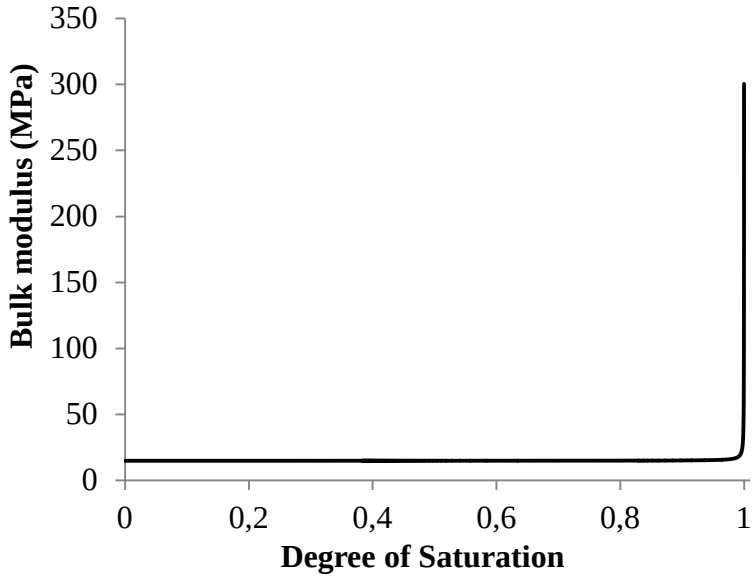

1019

1020 Figure 12. Variation of the unsaturated bulk modulus with the degree of saturation.

1021

1022

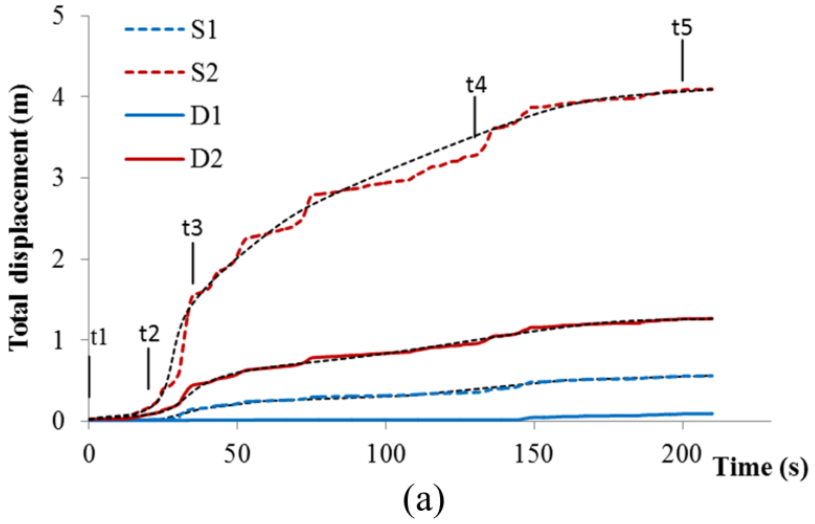

1023

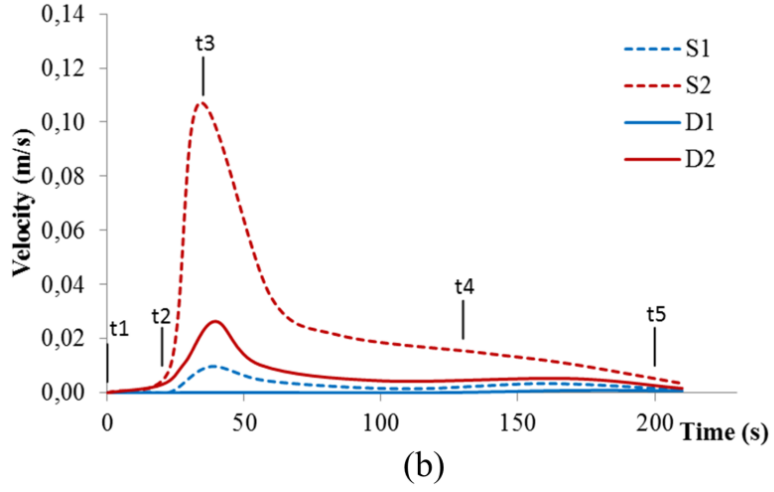

1024

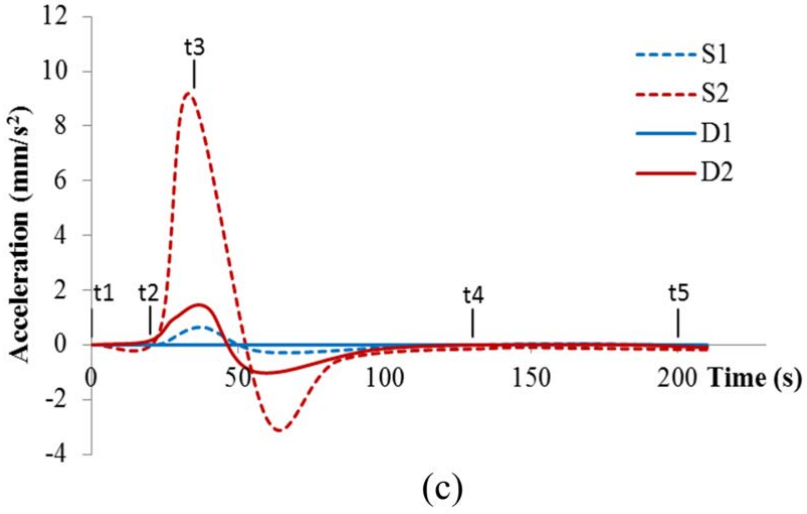

1025
1026 Figure 13. Evolution of (a) total displacement, (b) velocity and (c) acceleration of
1027 material points S1, S2, D1 and D2.

1028